Materials Today Bio 21 (2023) 100712

Contents lists available at ScienceDirect

Materials Today Bio

journal homepage: www.journals.elsevier.com/materials-today-bio

Ropivacaine microsphere-loaded electroconductive nerve dressings for long-acting analgesia and functional recovery following diabetic peripheral nerve injury

Fangguo Liang [a,1], Yusheng Yang [b,1], Yuyong Chen [c,1], Jiajun Xie [d,1], Shencai Liu [d], Zilin Tan [e], Liangjie Tian [b], Zhiqiang Yu [f], Zhanjun Shi [d,****], Peigen Xie [g,***], Hong Ding [h,**], Qinfeng Yang [d,*]

[a] Department of Plastic and Cosmetic Surgery, Nanfang Hospital, Southern Medical University, Guangzhou, Guangdong Province, 510515, China
[b] Division of Orthopaedics and Traumatology, Department of Orthopaedics, Nanfang Hospital, Southern Medical University, Guangzhou, Guangdong Province, 510515, China
[c] Department of Orthopedics, Southern University of Science and Technology Hospital, Shenzhen, Guangdong Province, 510800, China
[d] Division of Orthopaedic Surgery, Department of Orthopaedics, Nanfang Hospital, Southern Medical University, Guangzhou, Guangdong Province, 510515, China
[e] Department of General Surgery, Nanfang Hospital, Southern Medical University, Guangzhou, Guangdong Province, 510515, China
[f] Guangdong Provincial Key Laboratory of New Drug Screening, School of Pharmaceutical Sciences, Southern Medical University, Guangzhou, Guangdong, 510515, China
[g] Department of Spine Surgery, The Third Affiliated Hospital of Sun Yat-sen, University, Guangzhou, Guangdong Province, 510600, China
[h] Department of Anesthesiology, Nanfang Hospital, Southern Medical University, Guangzhou, Guangdong Province, 510515, China

ARTICLE INFO

Keywords:
Electroconductive hydrogel
Ropivacaine microspheres
Diabetic peripheral nerve injury
Analgesia
Nerve regeneration

ABSTRACT

In recent years, electroconductive hydrogels (ECHs) have shown great potential in promoting nerve regeneration and motor function recovery following diabetic peripheral nerve injury (PNI), attributed to their similar electrical and mechanical characteristics to innate nervous tissue. It is well-established that PNI causes motor deficits and pain, especially in diabetics. Current evidence suggests that ropivacaine (ROP) encapsulated in poly lactic-co-glycolic acid (PLGA) microspheres (MSs) yield a sustained analgesic effect. In this study, an ECH electroconductive network loaded with MS/ROP (ECH-MS/ROP) was designed as a promising therapeutic approach for diabetic PNI to exert lasting analgesia and functional recovery. This dual delivery system allowed ROP's slow and sequential release, achieving sustained analgesia as demonstrated by our *in vivo* experiments. Meanwhile, this system was designed like a lamellar dressing, with desirable adhesive and self-curling properties, convenient for treating injured nerve tissues via automatically wrapping tube-like structures, facilitating the process of implantation. Our *in vitro* assays verified that ECH-MS/ROP was able to enhance the adhesion and motility of Schwann cells. Besides, both *in vitro* and *in vivo* studies substantiated that ECH-MS/ROP stimulated myelinated axon regeneration through the MEK/ERK signaling pathway, thereby improving muscular denervation atrophy and facilitating functional recovery. Therefore, this study suggests that the ECH-MS/ROP dressing provides a promising strategy for treating diabetic PNI to facilitate nerve regeneration, functional recovery and pain relief.

1. Introduction

Peripheral nerve injury (PNI) is still a major cause of physical disability that may lead to different sensory and motor dysfunction levels, resulting in a reduced quality of life and a heavy burden on the healthcare system [1,2]. Peripheral nerve repair is often more challenging in diabetics attributed to long-term insulin resistance, hyperglycemia, and microvessel complications exacerbating axon degeneration, segmental demyelination, delayed regeneration of impaired nerves, and even denervated muscle atrophy [1,3,4]. Different

* Corresponding authors.
** Corresponding author.
*** Corresponding authors.
**** Corresponding author.
E-mail addresses: 18719096889@163.com (Z. Shi), xiepgen@mail.sysu.edu.cn (P. Xie), 107835301@qq.com (H. Ding), breezeyoung1@i.smu.edu.cn (Q. Yang).
[1] These authors contributed equally to this work.

https://doi.org/10.1016/j.mtbio.2023.100712
Received 6 April 2023; Received in revised form 15 June 2023; Accepted 19 June 2023
Available online 23 June 2023

approaches are indicated depending on the type and extent of PNI, including pharmaceuticals, decompression, neurorrhaphy, and grafting (allografts and autografts) [5–8]. However, pharmaceuticals alone play a negligible role in PNI repair since they are mainly used for symptom management with limited capacity to stimulate nerve regeneration and have shortcomings such as *in vivo* redistribution and rapid degradation [1,5,7,8]. Besides, surgery is also limited in the treatment of PNI, such as nerve decompression only focusing on alleviating further damage, neurorrhaphy leading to excessive tension, nerve grafting with limited supply, unavoidable mismatching size, and low achievement ratios of favorable functional recovery [4,6,7,9,10]. Given the challenge of repairing damaged nerves, especially for patients with diabetes mellitus (DM), novel strategies are required to effectively promote nerve regeneration [4,11,12].

The past few years have witnessed a burgeoning interest in biocompatible electroconductive hydrogels (ECHs) with electroconductive and soft mechanical properties compatible with endogenous nerve tissue to enhance neuronal differentiation and axonal regeneration [3,13–15]. It is widely acknowledged that electrical signals are crucial for nerve regrowth, remyelination and maturation in the innate nervous system [3,13–16]. Combining electrically conductive components with a hydrophilic matrix into the extracellular environment is able to promote the intercellular transduction of electric signals [3,13–15]. Thus, simulating the desirable electroconductive characteristics of the intrinsic nervous system is beneficial for nerve regrowth after PNI [3,13–15]. In previous reports, several soft, adhesive, conductive, and biocompatible ECHs were designed and could sufficiently stimulate neuronal and/or axon regeneration regrowth after PNI or spinal cord injury (SCI), consequently restoring motor function [3,13–15].

Nonetheless, there is an increasing consensus that PNI causes motor deficits and results in unbearable and sustained pain, including both inflammatory and neuropathic pain [7,17–21]. Worse, diabetic patients suffering PNI may exacerbate inflammatory pain due to the preexisting neuroinflammation [22,23]. Notwithstanding that electroconductive hydrogels have shown great potential in enhancing nerve repair, their *in vivo* application may lead to foreign body inflammatory responses, thereby exhibiting a limited ability to attenuate or even aggravate acute pain after PNI [15]. At present, pain after PNI can be managed by opioids, non-steroidal anti-inflammatory drugs (NSAIDs) and local anesthetics [17,18,20,24–26]. Nevertheless, long-term use of opioids and oral administration of NSAIDs will bring potential side effects [24–27]. Over the years, the application of local anesthetics during peripheral nerve block has gained significant popularity due to their superior analgesic effect with fewer complications and lower consumption of opioids [24–26]. Among these, ropivacaine (ROP) has a longer duration of action with lower cardio and neurotoxicity [26]. Nonetheless, local anesthetics require multiple administrations or continuous catheter infusion to achieve a sustained analgesic effect which may cause local adverse reactions such as dislodgement, leakage, infection, epidural hematoma and nerve impairment, and systemic toxicity [24–26]. Consequently, much emphasis has been placed on designing local anesthetics delivery systems with long-acting analgesics to minimize the associated side effects [24–26]. In recent years, polymer microspheres (MSs), specifically MSs prepared by poly lactic-co-glycolic acid (PLGA) with desirable biocompatibility, biodegradability, and stability during manufacturing and storage, have been employed extensively as carriers for local anesthetics to prolong analgesia [24,25,28,29]. Several studies have demonstrated that local anesthetics encapsulated by PLGA MSs exhibiting sustained release and lasting analgesia perform well against postoperative or neuropathic pain [24,25,28,29]. In this regard, there is an increasing consensus that combining hydrogels with MSs or nanoparticles yields a better analgetic effect since hydrogels can limit the diffusion of MSs or nanoparticles away from the lesion site [21,24–26].

Herein, we designed a MS/ROP-loaded ECH dressing, termed as ECH-MS/ROP, which showed outstanding electroconductivities, mechanical characteristics, biocompatibility, and prolonged release of local anesthetics to yield nerve regrowth, motor function restoration, and long-acting analgesia following diabetic PNI (Fig. 1). In this composite, ECH

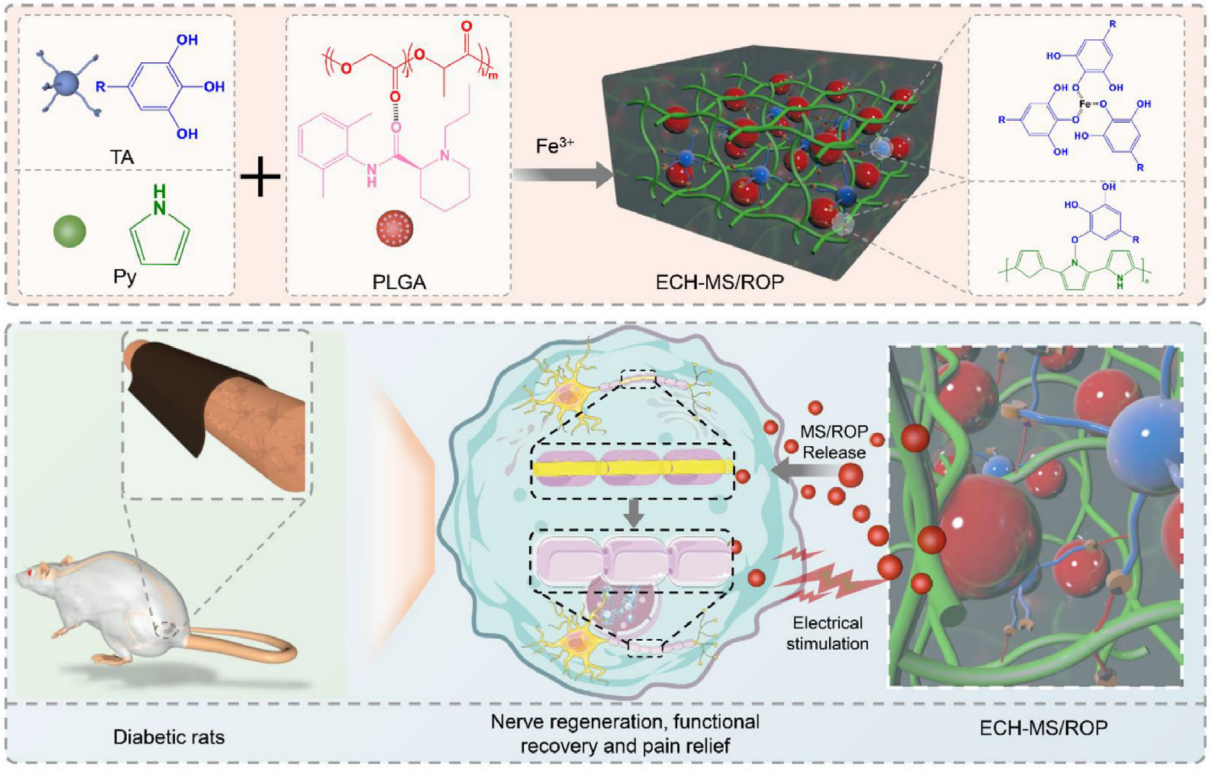

Fig. 1. The functional groups, chemical bonds and production of ECH-MS/ROP and its ability to promote nerve regeneration, functional restoration and pain relief after diabetic PNI.

consisted of polypyrrole (PPy) and tannic acid (TA) with soft, water-rich, porous, adhesive, and self-curling properties. Next, MS/ROP based on PLGA and ROP free base was embedded in the ECH network. We detected this composite's micromorphological, mechanical, electrical, and drug-release properties. Subsequently, the *in vitro* cell biocompatibility, attachment, migration, and neurite elongation of Schwann cells and/or PC-12 cells on this composite were evaluated. Furthermore, nerve regrowth, functional restoration and prolonged pain relief were assessed in a diabetic sciatic nerve injury model to examine the dual therapeutical effect of ECH-MS/ROP.

2. Materials and methods

2.1. Fabrication of ROP-loaded PLGA MS

MS/ROP was prepared via emulsion-solvent evaporation in accordance with prior protocols with minor modifications [24,25,28,29]. Briefly, 100.0 mg of ROP (Accela, Shanghai, China) and 100.0 mg of PLGA (Birmingham Polymers, Birmingham, USA) were dissolved in 2.0 mL of dichloromethane (DCM, Aladdin, China), followed by sonication for 1 min until complete dissolution, as an organic oil phase. This mixture was dropwise transferred to 20.0 mL of 1.5% (W/V) Polyvinyl alcohol (PVA, Aladdin, China) solution for further mixing evenly under a high-speed shearing machine (IKA, Germany) at 2000 rounds per minute (rpm) for 2 min. Then, the acquired emulsion was directly mixed with 60.0 mL of 0.5% (W/V) PVA aqueous solution, followed by stirring for 6–8 h for evaporating DCM. Subsequently, the solidified MS/ROP of which diameter exceeded 100 μm was removed through a standard sifter. After centrifugation at 4500 rpm for 5 min, the remaining MS/ROP was collected and washed thrice with deionized (DI) water for purification, followed by lyophilizing for subsequent use.

2.2. Examination of drug loading content (DLC) of MS/ROP

The DLC was determined by ultraviolet–visible (UV–vis) spectroscopy [24,25]. Briefly, 50.0 mg of ROP was accurately weighed and dissolved in a 100.0 mL volumetric flask, adding methanol to form an ROP solution (0.5 mg/mL). Next, a series of ROP solutions of different concentrations were prepared to measure the corresponding absorption values at 245 nm using a UV–vis spectrometer (ThermoFisher Scientific, USA). A calibration curve was obtained by linear regression of ropivacaine concentration versus the absorption value utilizing Origin 2022. Next, 1.0 mL of DCM was used to dissolve 10.0 mg of MS/ROP. Samples were ultrasonicated to split MS/ROP and diluted with methanol to a final volume of 10.0 mL. After centrifugation of the mixed solution at 4500 rpm for 5 min, the supernatant was collected. Finally, the concentration of ROP was acquired based on the calibration curves by detecting the absorption value at 245 nm. DLC was calculated based on formula (1).

$$\text{DLC}\ (\%) = \frac{W_{ROP}}{W_{MS/ROP}} \times 100\% \quad (1)$$

where W_{ROP} indicates the weight of ROP in MS/ROP, and $W_{MS/ROP}$ represents the weight of MS/ROP.

2.3. Fabrication of ECH

Based on our prior synthesis procedure, 4 mg of TA (Aladdin, China) was first weighed and dissolved in 0.6 mL of DI water. Subsequently, 35 μL (equal to 0.5 mmol) of pyrrole (Py, 99%, Aldrich, St. Louis, USA) was mixed with the aforementioned TA solution and stirred for the production of solution I. Next, 0.6 mL of DI water was used to dissolve 0.316 g of ferric chloride hexahydrate ($FeCl_3{\cdot}6H_2O$, 98%, Aladdin, China) powder to prepare Solution II. Further, gelation was induced by mixing Solutions I and II at 4 °C. Finally, the hydrogels were purified by immersing them in DI water overnight [3,13].

2.4. Fabrication of ECH-MS/ROP system

According to the effective dose (12 mg/kg) of ROP applied in rats from the literature, 75 mg lyophilized MS/ROP powder was mixed with solution I and stirred to obtain solution III [28,29]. Similarly, solutions II and III were mixed gently at 4 °C for gelation.

2.5. Characterization of ECH-MS/ROP hydrogel

2.5.1. Scanning electron microscopy (SEM)

The detection of samples' morphology was performed by utilizing SEM (ZEISS Ultra 55, Germany) at 10 kV accelerating voltage [3,15,30]. The hydrogels were freeze-dried and sputter-coated with platinum (Pt) for subsequent visualizing scan.

2.5.2. Fourier transform infrared spectroscopy (FTIR)

The chemical composition and functional groups of the samples were examined using a Nicolet IS10 spectrometer (Thermo Scientific, USA) over 32 scans at a 4 cm^{-1} resolution [3,13,15,30]. After lyophilization of samples, they were pulverized and pressed into tablets. The results were recorded by the corresponding spectrum software.

2.5.3. Rheological experiments

The rheological properties of the samples were determined by a rotary rheometer (Physician MCR301, Anton Paar, Austria) [3,13,30]. A constant strain of 1% was set for the angular frequency sweep from 0.1 Hz to 10 Hz. The acquisition of elastic modulus (storage modulus, G′) and viscous modulus (loss modulus, G″) were obtained from the typical regions of frequency-modulus curves, respectively.

2.5.4. Electrical properties

The characterizations of the conductive properties of hydrogels, which includes the cyclic voltammetry (CV) and electrochemical impedance spectroscopy (EIS), were achieved by an electrochemical workstation (Zennium Zahner, Germany) [3,13–15,30]. These tests required a counter electrode (platinum) and a reference electrode (Ag/AgCl). Samples were immobilized on the indium tin oxide (ITO) glass as a working electrode was prepared by, which was immersed into an electrolyte solution of phosphate-buffered saline (PBS) (pH = 7.4, 0.1 M). The CV experiments were carried out with a sweep rate of 10 mV/s and a potential between −0.8 V to 1.0 V. This three-electrode system was used to assess the EIS spectra with a fixed amplitude of 5 mV and a frequency from 1×10^{-2} Hz to 1×10^{6} Hz.

2.5.5. Spatial distribution of MS/ROP in the ECH-MS/ROP

MS, ROP and ECH were first labeled by rhodamine B (RhB, Aladdin, China), fluorescein isothiocyanate (FITC, Aladdin, China), and diamidino phenylindole (DAPI, Beyotime, China), respectively, and visualized under a confocal laser scanning microscopy (Leica TCS SP8, Germany) [24,25]. To prepare the RhB-labeled MS, 0.2 mg of RhB and 100.0 mg of PLGA were dissolved in 1.0 mL of DCM. To prepare the FITC-labled ROP, 0.2 mg of FITC 100.0 mg of ROP were dissolved in 1.0 mL of DCM. Next, the solution of RhB-labeled MS and FITC-labled ROP was mixed and the labeled MS/ROP was synthesized via an emulsion-solvent evaporation method in the dark. For preparation of the DAPI-labled ECH, 0.2 mg of DAPI and 4 mg of TA was dissolved in 0.6 mL of DI water and the labeled ECH was fabricated as described above (in the dark). Finally, the spatial distribution of MS/ROP in the labeled ECH-MS/ROP was observed.

2.5.6. In vitro release characteristics of ROP

A direct release approach was used to determine the release characteristics of ROP from MS/ROP and ECH-MS/ROP [24,25]. In brief, the MS/ROP powder (75 mg) and ECH-MS/ROP dressing (75 mg MS/ROP) were separately incubated in 5.0 mL of PBS. The centrifuge tubes were then shaken at 37 °C at 70 rpm. The supernatant was collected at specified intervals within 8 days and stored at 4 °C for further measurement

after centrifugation at 4500 rpm for 5 min. An isometric fresh PBS was added to the centrifuge tubes and incubated. The amounts of ROP released into the supernatant were measured via ultraviolet–visible (UV–vis) spectroscopy.

2.6. In vitro experiments

2.6.1. Preparation and culture of rats dorsal root ganglion (DRG), Schwann cells, and PC-12 cells

DRGs were extracted from 3-day old Sprague Dawley (SD) rats. Briefly, after horizontal dissection of spinal canal, the DRGs were isolated, followed by membrane peeling under a stereomicroscope. The DRGs were cultured on the standard glass slide, ECH, and ECH-MS/ROP, respectively, with specific culture medium containing neurobasal-A (Gibco, USA), 50 ng/mL nerve growth factor (NGF, PeproTech, USA), 1 × B-27 supplement (Gibco, USA), 1 × penicillin/streptomycin (Gibco, USA), and 1×glutamine (Gibco, USA) at 37 °C under 5% CO_2 [3]. Schwann cells and PC-12 cells were acquired from the ATCC (Manassas, USA) and cultured in high glucose Dulbecco's modified Eagle's medium (DMEM, Gibco, USA) supplemented with 10% fetal bovine serum (FBS, Gibco, USA) under an identical atmosphere to the DRGs.

2.6.2. Cell biocompatibility and viability evaluation

The *in vitro* biocompatibility of each sample was assessed by the live/dead staining, cell counting kit-8 (CCK-8, Beyotime, China), and cytoskeletal staining assays [3,15,30]. For the live/dead staining assay, 5 × 10^5 Schwann cells and PC-12 cells were separately co-cultured with each sample for 24 h. After that, each sample was co-incubated with the live/dead working solution, including PBS, Calcein-AM (Invitrogen, USA), and propidium iodide (PI, Invitrogen, USA) for 30 min. The results were visualized under a confocal reflection microscope (ZEISS LSM 980, Germany). To assess the proliferation of Schwann cells and PC-12 cells of each group for 1, 3, and 7 days, a concentration of 100 μL/mL CCK-8 solution (Beyotime, China) was prepared and then supplemented into each well with a density of 5 × 10^5 cells for incubating for 2 h. Next, an enzyme labeling instrument (BioTech, Germany) was applied to detect the optical density (OD) value of each group at 450 nm wavelength after 100 μL of suspension was transferred into a 96-well plate. The cytoskeletal staining assay was detected after 1 × 10^5 cells (Schwann cells or PC-12 cells) were seeded on each sample for 3 days. After fixation with 4% paraformaldehyde and staining with Actin Tracker Green (Beyotime, China) and Hoechst (Beyotime, China), the images were captured by a laser confocal reflection microscope (ZEISS LSM 980, Germany).

2.6.3. Artificial wound for cell migration assay

It has been universally acknowledged that the migration of Schwann cells is vital for successful peripheral nerve repair as migrating Schwann cells form a cord in the nerve bridge, generate a regenerative microenviroment, support the axons metabolism, affect the myelination process and guide axon regeneration [3,31–33]. Therefore, to investigate the cell motility ability on each sample, an artificial wound was made by creating a longitudinal scratch after the Schwann cells approximately reached a confluence of 90% and cultured for 12 h and 24 h [3,30]. Then, the detached cells were removed by washing with PBS thrice. Finally, after staining with Calcein AM (Invitrogen, USA), the graphs were captured by a laser confocal reflection microscope (ZEISS LSM 980, Germany).

2.6.4. Gene expression

First, a total RNA extraction kit (Omega, USA) was used to obtain the total RNA [3,15,30]. Next, cDNA was acquired by reversely transcribed total RNA with a reverse transcription kit (Thermo Fisher, USA) for real-time qPCR (RT-qPCR) on the QuantStudio 5 (Thermo Fisher, USA). This assay was conducted thrice before analysis via the $2^{-\Delta\Delta Ct}$ approach. The primers used for each gene are presented in Table 1.

Table 1
Primer sequences of each gene.

Target	Forward	Reverse
GAPDH	AGACAGCCGCATCTTCTTGT	CTTGCCGTGGGTAGAGTCAT
NF	GTTCCGAGTGAGGTTGGACC	CCGCCGGTACTCAGTTATCTC
GAP43	GCACATCGGCTTGTTTAGGCT	GGAGGGAGATGGCTCTGCTACT
TUJ1	CCCGTTTTAGCCACCTTTGTATT	CCCTCCAAATATAAACACAACCC
SYN	CTTCCTGGTTGGGGACTACTCCTC	GCGAACACGGCTGTAGCCAGAAAG

2.6.5. Immunofluorescence (IF) assay

To carry out the IF assay, cells or tissues were first fixed in 4% paraformaldehyde for 30 min. Subsequently, they were immersed in 0.5% Triton X-100 (Biofroxx, Germany) for 20 min for permeabilization and blocked by 3% bovine serum albumin (BSA, Biofroxx, Germany) for 60 min at room temperature. Then, specific primary antibodies was prepared and added into the samples for reaction overnight at 4 °C (Table 2). Secondary antibodies were added for further reaction for 60 min at room temperature. Ultimately, the nuclei were stained with Hoechst 33342 (Beyotime, China), followed by visualization under a laser confocal microscope (ZEISS LSM 980, Germany) [3,15,30].

2.6.6. Western blot (WB) experiment

To extract proteins, cells or the harvested tissues were first dissolved in a radio-immunoprecipitation assay (RIPA, CWBIO, China) buffer supplemented with phosphatase and protease inhibitors (Thermo Fisher, USA) on ice for 30 min. The supernatant was harvested and preserved at −20 °C for further utilization after centrifugation at 4 °C. The BCA assay kit (Beyotime, China) was applied to measure the total protein concentration. Protein was denatured by heating at 100 °C for 10 min. Next, equal amounts (40 μg) of protein were added to sodium dodecyl sulfate-polyacrylamide gel electrophoresis (SDS-PAGE) and then transferred onto the polyvinylidene difluoride (PVDF, Thermo Fisher, USA) membranes. After blocking with 5% non-fat milk for 60 min, the PVDF membranes were incubated with the primary antibodies (Table 2) overnight at 4 °C and respective secondary antibodies for 1 h. An enhanced chemiluminescence (ECL, Thermo Fisher, USA) kit was applied to visualize the protein bands. Finally, the images were captured by the GelView 6000 Pro (BLT, China) and quantified utilizing ImageJ software [3,15,30].

2.7. In vivo experiments

2.7.1. Ethics statement

All animal experiments were conducted in compliance with the requirements of the National Institutes of Health Guide for the Care and Use of Laboratory Animals after obtaining the approval of the Animal Experimental Ethics Committee of Southern Medical University Nanfang Hospital.

2.7.2. Establishment of diabetic sciatic nerve crush injury model

Adult male SD rats (weight 320–360 g) were utilized in the present study. As previously documented, rats were intraperitoneally injected with streptozotocin (STZ) solution at 70 mg/kg for the establishment of a diabetic model [3]. A random blood glucose concentration above 16.7 mmol/L indicated DM based on current guidelines [3,34]. 27 rats with DM were randomly assigned to three groups; the PNI group (n = 9), the ECH group (n = 9), and the ECH-MS/ROP group (n = 9). Fig. S1 provides the details on the weight and blood glucose values of each group.

Xylazine (5 mg/kg) and ketamine (70 mg/kg) were mixed for anesthesia of the diabetic rats via intraperitoneal injection. The establishment of diabetic sciatic nerve crush injury model was based on previously described surgical protocols [3,4,26,35]. After skin incision (1.5 cm) on the left thigh, the sciatic nerve was exposed by a blunt dissection of the gluteal muscle. Two vascular clips (30 g force for 120 s) were used to induce sciatic nerve (0.5 cm near to the sciatic notch) crush injury. The

Table 2
Information about primary antibodies used in the present study.

Antibodies	Species	Type	Dilution (IF/WB)	Source
Anti-GAPDH	Rabbit	Monoclonal lgG	1:1000	CST, America
Anti-Neurofilament (NF)	Rabbit	Polyclonal lgG	1:200/1:1000	ProteinTech, China
Anti-Growth-associated protein-43 (GAP43)	Rabbit	Polyclonal lgG	1:2000	ProteinTech, China
Anti-Myelin basic protein (MBP)	Rabbit	Polyclonal lgG	1:2000	ProteinTech, China
Anti-S100 beta (S100)	Rabbit	Polyclonal lgG	1:1000	ProteinTech, China
Anti-MEK1/2	Mouse	Monoclonal lgG	1:1000	CST, America
Anti-Phospho-MEK1/2 (Ser217/221)	Rabbit	Monoclonal lgG	1:1000	CST, America
Anti-p44/42 MAPK (Erk1/2)	Rabbit	Monoclonal lgG	1:1000	CST, America
Anti-Phospho-MAPK (Erk1/2) (Thr202/ Ty204)	Rabbit	Monoclonal lgG	1:1000	CST, America

PNI group only experienced nerve impairment without any treatment. In the two treatment groups, ECH and ECH-MS/ROP were implanted around the injured nerve and automatically wrapped tubular structures, respectively. Finally, the muscle and skin layer were sutured successively and intermittently by 4/0 Mersilk sutures. The right hind limb of the animal was regarded as the nonoperative control. After the surgery, the rats were well-fed and kept warm.

2.7.3. Analysis of mechanical allodynia

Based on previously documented approaches, a rat was placed in an individual chamber on a metal mesh and allowed to adapt to the environment for 1 h before testing [36–39]. Mechanical allodynia was determined by measuring the paw withdrawal threshold (PWT) with ascending forces induced by von-Frey filaments (4, 6, 8, 10, 15, 26, 60, 100, and 180 g). Positive responses were recorded when the force elicited the withdrawal, biting or licking of the posterior paw. Five repeated stimulations were conducted for each rat at a 60-s interval. This experiemt was performed before (6 h) and after the operation at predefined time points (12, 24, 36, 48, 60, 72, 84, 96, 108, 120, 144, 168, and 192 h). PWT was measured twice daily from day 1 to day 5 and once daily from day 6. An increase of PWT represented a reduction in mechanical allodynia or pain easement. A schematic illustration portraying this experiment is shown in Fig. 6A.

2.7.4. Accessment of thermal hyperalgesia

Thermal hyperalgesia could be evaluated via a hot plate experiment which was modified based on prior researches [26,37]. Briefly, the rats were placed in an individual chamber on a thermally conductive floor, then their posterior paws were allowed to touch a heated plate warmed to 56 °C. Thermal withdrawal latency (TWL) was recorded as the time the animals took to raise or lick their hind paws. The animals were acclimated 1 day before the procedure to evaluate and identify the baseline of TWL. This assay was performed before (4 h) and after surgery (12, 24, 36, 48, 60, 72, 84, 96, 108, 120, 144, 168, and 192 h). Correspondingly, TWL was measured twice daily from day 1 to day 5 and once daily from day 6. The assays performed prior to the operation (4 h) served as the TWL baseline. Similarly, five repeated exposures were performed for each animal and the mean value was adopted. The tests were conducted at 1-min intervals to prevent tissue scald. Consistently, an increase of TWL indicated a decrease in thermal hyperalgesia or pain easement. A schematic illustration portraying this experiment is shown in Fig. 6D.

2.7.5. Evaluation of motor function

The walking track measurement carried out 2, 3, and 4 weeks after the surgery was used to evaluate the motor function restoration [3,30]. After coating the posterior paws of the rats in non-toxic blue ink, they were allowed to walk from one end to the other end of the sidewalk. The distances of footprints, which included print length (PL, distance between the third toe to the heel), toe spread (TS, distance between the first to the fifth toe), and intermediate toe spread (ITS, distance between the second to the fourth toe) were measured for to calculate the sciatic function index (SFI). A schematic illustration displaying the measured footprint parameters is shown in Fig. 6G. The following formula was used to calculate the SFI (2):

$$\mathrm{SFI} = -38.3 \times \frac{(\mathrm{PL}_{\mathrm{Exp}} - \mathrm{PL}_{\mathrm{Ctrl}})}{\mathrm{PL}_{\mathrm{Ctrl}}} + 109.5 \times \frac{(\mathrm{TS}_{\mathrm{Exp}} - \mathrm{TS}_{\mathrm{Ctrl}})}{\mathrm{TS}_{\mathrm{Ctrl}}} + 13.3 \times \frac{(\mathrm{ITS}_{\mathrm{Exp}} - \mathrm{ITS}_{\mathrm{Ctrl}})}{\mathrm{ITS}_{\mathrm{Ctrl}}} - 8.8 \quad (2)$$

where Ctrl and Exp indicate the control and experimental sides, respectively.

2.7.6. Evaluation of hemocompatibility and in vivo biocompatibility

To evaluate the hemocompatibility of samples, they were separately co-incubated with fresh whole blood collected from rats at 37 °C for 4 h. A negative and a positive group were set by adding PBS and Triton-100X, respectively. After centrifugation at 10,000 g for 5 min at 4 °C, the supernatant was added to a 96-well plate, and the absorbance was measured at 540 nm by an enzyme-labeling instrument (BioTech, Germany) [3,14,30]. The following equation was applied for the calculation of hemolysis percentage (3):

$$\mathrm{Hemolysis}\ (\%) = \frac{\mathrm{OD}_{\mathrm{Sample}} - \mathrm{OD}_{\mathrm{PBS}}}{\mathrm{OD}_{\mathrm{Triton}} - \mathrm{OD}_{\mathrm{PBS}}} \times 100\% \quad (3)$$

where OD indicates the optical density.

In addition, the levels of biochemical parameters which includes alanine aminotransferase (ALT), aspartate aminotransferase (AST) and total protein (TP) were measured to detect the *in vivo* biocompatibility of materials after collecting whole blood from 4-weeks treated rats. Main organs, including the heart, lung, liver, spleen and kidney, were stained by hematoxylin-eosin (H&E) for histological analysis [3,14,30].

2.7.7. Morphological evaluation for gastrocnemius muscle and sciatic nerve

After 4 weeks of treatment, animals were under deep anesthesia after injection of 0.6% sodium pentobarbital and then were sacrificed. Gastrocnemius muscles and regrown nerve fibers and were dissected, followed by fixing in 4% paraformaldehyde for 24 h before embedding in paraffin. Nerve tissues were longitudinally embedded in paraffin for better morphological observation. Next, 10 μm-thick slices were cut followed by staining with H&E and Masson trichrome staining (MTS). Besides, HE and MTS were also used to stain 30 μm-thick transverse sections of ipsilateral gastrocnemius muscles to observe their histological changes [3,30]. The images of each tissue were captured using a slide scanner.

2.7.8. Axon myelination assessment

To assess the axon myelination, toluidine blue staining (TBS) and transmission electron microscopy (TEM) were performed to observe the middle regions of regenerated nerves harvested 4 weeks after surgery [3,30]. Epoxy resin was used to embedd the samples after dewaxing. Next, samples were cut into semi-thin (1 μm) transverse sections for TBS and ultrathin (50 nm) transverse sections for TEM (HT7700, Japan).

2.8. Statistical analysis

Statistical analyses were performed utilizing GraphPad Prism 8 software (GraphPad Software, USA) and SPSS version 23 (IBM, USA). All quantitative data were presented as mean ± standard deviation (SD). Groups were compared by unpaired t-tests (two groups) or one-way analysis of variance (ANOVA) with Bonferroni's test (three or more groups) when data were normally distributed. Groups were compared by the Kruskal-Wallis test when data were nonparametric. A P-value <0.05 was statistically significant.

3. Results and discussion

3.1. Synthesis of ECH-MS/ROP composite

Fig. 2A depicts the material synthesis process and brief chemical constitution of the ECH-MS/ROP. The ROP-encapsulated MS was prepared by emulsion solvent evaporation, followed by lyophilizing to obtain white powders. The DLC of MS/ROP acquired via a UV–vis method was approximately 41 wt%. The ECH was formed via rapid gelation within 2 s due to the crosslinking of TA and PPy after supplementation of $FeCl_3$ (oxidative initiator). The phenol hydroxy groups on TA and the protonated nitrogen groups on PPy produce intermolecular electrostatic interactions to facilitate this crosslinking. Furthermore, it has been established that TA acts as a dopant due to that it protonates the nitrogen groups of PPy to be electroconductive [3,13]. Interestingly, Fe^{3+} promotes the gelation process since the Fe^{3+} ions enable the Py to polymerize via oxidation and further ionically crosslinks with TA [3,13]. Notably, this dual and specific function of Fe^{3+} ions cannot be replaced by other metallic ions, such as magnesium. Although magnesium has been reported to effectively facilitate nerve repair by enhancing nerve regeneration, angiogenesis and blood supply, it can only act as an ionic crosslinker and cannot promote the gelation process of ECH due to the lack of oxidation ability to facilitate the polymerization of Py [3,13,40–42]. In addition, to verify the significance of Fe^{3+} ions, previous study had used ammonium peroxydisulfate (APS) as an oxidant instead of $FeCl_3$, which was unable to form gelatin due to the lack of ionic crosslinker [13]. Finally, the MS/ROP is entrapped into the hydrogel internal network to form the ECH-MS/ROP composite by mixing the MS/ROP powders with TA-Py solution and Fe^{3+} solution for gelation.

3.2. Characterization of ECH-MS/ROP composite

The FTIR spectrum of the ROP exhibited several characteristic peaks. The peaks at 3200 cm^{-1} and 1650 cm^{-1} corresponded to N–H stretching and C═O of the amide bond, respectively (Fig. 2B) [43,44]. Besides, the peaks at 1600, 1580, and 1450 cm^{-1} could be attributed to the benzene ring group (stretching and bending vibrations of the C–H) (Fig. 2B) [43]. The typical peaks in the PLGA-MS spectrum could be observed at 3000, 1760, and 1175 cm^{-1}, corresponding to the stretching vibrations of C–H, C–O, and C–O–C, respectively (Fig. 2B) [45,46]. The MS/ROP spectrum was similar to that of the ROP and PLGA-MS, indicating that the MS/ROP was successfully prepared (Fig. 2B). As shown in Fig. 2C, the ECH spectrum was almost identical to the pristine PPy, suggesting that PPy is a major component of this hydrogel. Since PPy possesses outstanding electroconductive properties and biocompatibility, it is widely applied in neural tissue engineering. Besides, PPy polymer has been reported to improve neuronal activity and promote neuronal outgrowth [13]. The stretching vibrations of the C–N^+ bonds and C═N^+−C bonds were observed at 1174 cm^{-1} and 903 cm^{-1} in the ECH spectrum respectively (Fig. 2C), confirming a highly mixed level in the ECH [3,13]. Finally, the characteristic peaks of the main groups and bonds could be seen in the ECH-MS/ROP spectrum (Fig. 2D), implying the successful embedment of MS/ROP into the ECH network.

It is noteworthy that the addition of MS/ROP did not affect the crosslinking and gelation time (within 2 s) of ECH (Fig. 2E). SEM imaging showed that MS/ROP (7.15 ± 2.30 μm) exhibited round spheres with a nonporous and smooth surface, while ECH exhibited a 3D highly porous structure and interconnected globular nanoparticles of PPy on the surface (Fig. 2F–G) [15]. Furthermore, MS/ROP was successfully embedded within the porous ECH and still maintained their round morphology (Fig. 2H). The porous network in ECH not only provided favorable space for nerve cell penetration, adhesion and extension but also effectively limited the diffusion of MS/ROP away from the lesion site [3,13,15].

ROP encapsulated in MS with or without hydrogel loading was evaluated to examine whether ECH could prolong drug release. MS/ROP and ECH-MS/ROP could release ROP into PBS solution when placed in a shaking incubator at 37 °C at 70 rpm for 8 days. The cumulative release profiles of ROP from MS/ROP and ECH-MS/ROP are exhibited in Fig. 2I. Briefly, biphasic *in vitro* release profiles of ROP from MS/ROP were observed, containing an incipient rapid release and a subsequent gradual release. 29.64% of the drug were released from MS/ROP within the first 24 h. In contrast, ROP was released more stably from the ECH-MS/ROP composite, with a significantly diminished rapid release rate of 20.36% within the first 24 h ($P < 0.01$). Furthermore, over 8 days, a sustained release of 60.36% in the ECH-MS/ROP composite and 74.83% in the MS/ROP implied that the porous ECH network could prolong the delivery of local anesthetics. During the first phase (within 24 h), the increase in the initial release of MS/ROP could be attributed to the presence of ROP near or on the surface of MS, which diffused rapidly once immersed in the external liquid. Nevertheless, for the ECH-MS/ROP delivery system, MS/ROP was maintained in the matrix of ECH and the release of the ROP molecules dispersed in the ECH was further slowed by the surrounding hydrogel matrix, thereby preventing the rapid release [25,47]. During the second phase (after 24 h), the steady and slow drug release was attributed to the diffusion from the MS and the outer hydrophilic ECH [25,47].

To further detect the 3D distribution of MS/ROP in the ECH-MS/ROP system, MS, ROP and ECH were labeled by RhB, FITC and DAPI, respectively. As exhibited in Fig. 2J, the MS/ROP with red and green fluorescence was spatially and evenly distributed in the ECH with blue fluorescence. Hence, this result revealed that the ECH could effectively load MS/ROP and was beneficial for the *in situ* prolonged delivery of ROP [24,25].

It is well-established that cellular development, differentiation and fate are affected by the mechanical characteristics of extracellular matrix [3,13,14]. Dynamic oscillatory frequency sweep tests were used to examine the mechanical characteristics of ECH and ECH-MS/ROP. The storage modulus (elastic modulus G′) of these two hydrogels was larger than the loss modulus (viscous modulus G″) with an angular frequency ranging from 0.1 Hz to 10 Hz, indicating that both hydrogels have outstanding stability and viscoelasticity (Fig. 2K). Additionally, the mean storage moduli of ECH-MS/ROP (842 ± 76 Pa) were smaller than ECH (991 ± 6 Pa) (Fig. 2L), implying that the loading of MS/ROP slightly affected the mechanical characteristics of hydrogel. These results substantiate that the mechanical characteristics of ECH with or without MS/ROP are identical to normal nervous tissue (100–3000 Pa), which provide a favorable mechanical microenvironment and flexibility for axon extension [3,13–15].

Our prior research illustrated that electroconductive hydrogels could benefit SCI or PNI repair through facilitating the transmission of endogenic bioelectric signals [3,13–15]. Consequently, an electrochemical workstation was applied to investigate the electroconductive properties of ECH and ECH-MS/ROP. No current could be seen in the pure ITO

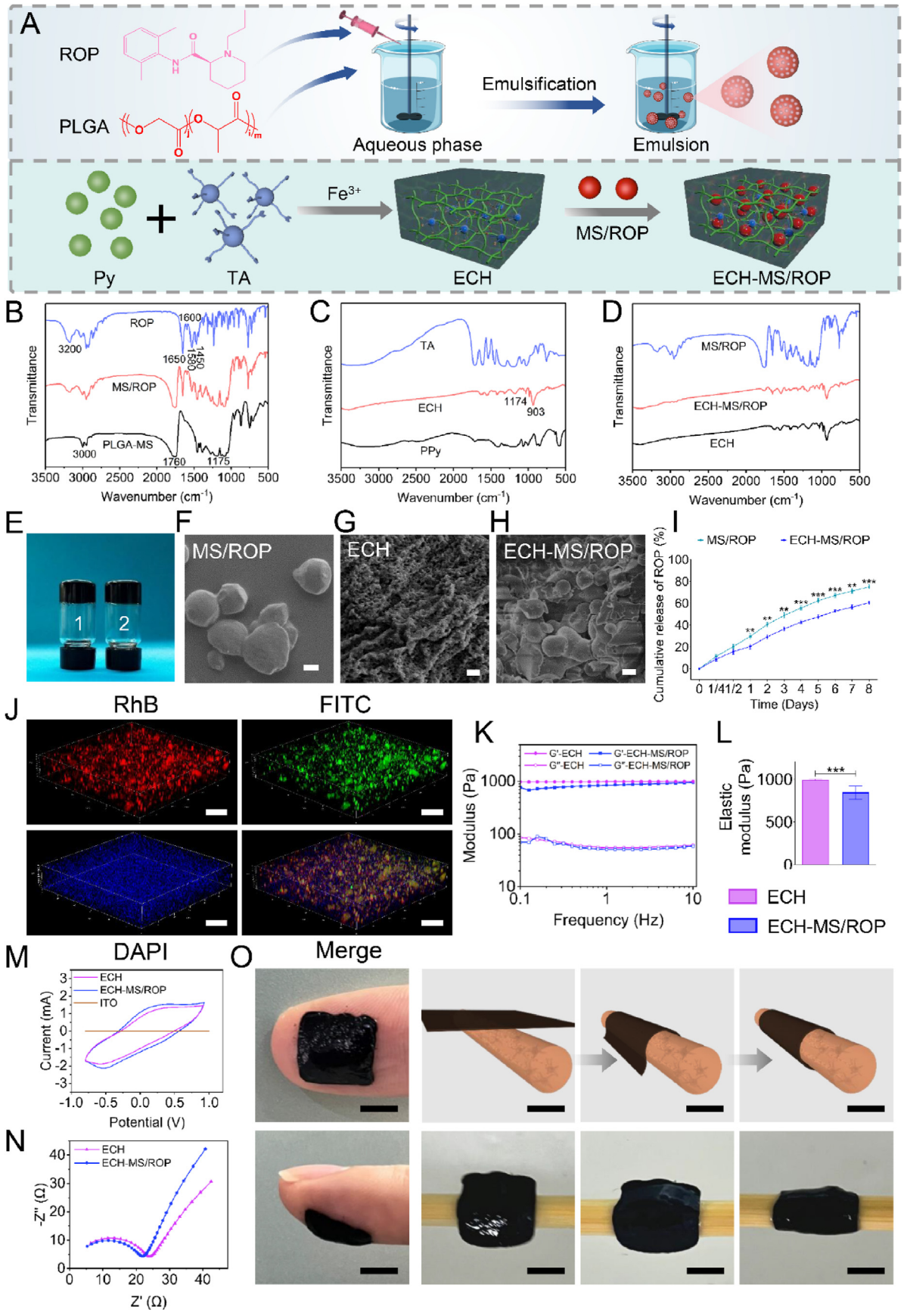

(caption on next page)

Fig. 2. Characterization of the ECH-MS/ROP composite. (A) Illustration of the fabrication and structure of the ECH-MS/ROP composite. (B) FTIR spectra of ROP (blue), PLGA-MS (black), and the MS/ROP (red). (C) FTIR spectra of TA (blue), PPy (black), and ECH (red). (D) FTIR spectra of MS/ROP (blue), ECH (black), and the ECH-MS/ROP (red). (E) Photographs showing the occurrence of gelation with or without MS/ROP, Vial 1 indicates ECH and Vial 2 indicates ECH-MS/ROP. (F) The microstructure of the MS/ROP was visualized under SEM. Scale bar: 2 μm. (G) The microstructure of the ECH was observed under SEM. Scale bar: 10 μm. (H) The microstructure of the ECH-MS/ROP system was detected by SEM. Scale bar: 10 μm. (I) The cumulative release curve of ROP from PLGA-MS with or without ECH until day 8 (n = 3). (J) Fluorescent images of labeled ECH-MS/ROP. Red, green and blue fluorescences suggest RhB-labeled MS, FITC-labeled ROP and DAPI-labeled ECH, respectively. Scale bar: 50 μm. (K) Mechanical properties of ECH and ECH-MS/ROP. (L) Graph of the quantification of rheological properties of ECH with or without MS/ROP (n = 5). (M) Cyclic voltammograms of ECH with or without MS/ROP. (N) Nyquist curves of ECH and ECH-MS/ROP. (O) Illustrations and photographs showed adhesive and self-curling ECH-MS/ROP as a laminar dressing that adhered to the finger and automatically wrapped a size-matched tubular structure. Scale bar: 500 mm. Statistical differences were determined by using One-way ANOVA with Bonferroni's multiple comparison tests when comparing three or more groups. When comparing two groups, the unpaired *t*-test was used. (*$P < 0.05$, **$P < 0.01$, and ***$P < 0.001$). (For interpretation of the references to colour in this figure legend, the reader is referred to the Web version of this article.)

electrode, while the ECH and ECH-MS/ROP exhibited significant anodic and cathodic currents given by the conductive capacities of PPy (Fig. 2M). Furthermore, current values of these two hydrogels were highly consistent regardless of oxidation and reduction reaction, which suggested that the crosslinking density and doping levels were not influenced by the loading of MS/ROP, thus displaying analogous electroconductivity (Fig. 2M). EIS tests were also performed to evaluate the electrical conductivities of two hydrogels. In the Nyquist plots, a quasi-semicircle was observed in the high-frequency region for both ECH and ECH-MS/ROP, implying satisfactory redox activity (Fig. 2N). Besides, the quasi-semicircle diameter of ECH and ECH-MS/ROP was comparable, suggesting that the charge transfer resistance would not the change with the embedment of MS/ROP. These results coincided with the CV analyses (Fig. 2N). It is well acknowledged that the quasi-semicircle diameter is positively correlated to the charge transfer resistance. Therefore, a smaller semicircle diameter indicates a smaller charge transfer resistance. Interestingly, the quasi-semicircle diameter of these two hydrogels was slightly smaller than in our prior studies, implying a disparity in charge transfer resistance. It is well-established that great conductive properties (low resistance) are highly beneficial for quick cell-to-cell communication through intrinsic bioelectric signals produced by the ion channels or pumps between neighboring cells [3,13–15].

Moreover, the ECH-MS/ROP composite could attach to irregularly shaped substances such as fingers and chopsticks (Fig. 2O). This adhesive nature of ECH-MS/ROP suggests it can be designed to be a laminar dressing to adhere to nerve tissue, followed by automatically wrapping and forming tubular structure with matched size, which makes the inconvenient installation process of neural materials to be simple, especially for diabetics (Fig. 2O). Indeed, for effective fixation of scaffolds, they must be sewned up with residual nerve tissues during repair of injured nerves [3,5,48]. In addition, the porous structure and hydrophilicity of the ECH-MS/ROP are essential for outstanding adhesion to endogenous nerve fiber [3]. Besides, in the self-curling process, the hydrogel can contact mutually through end-to-end and rapidly reforming an integral tube-like wrap structure due to the coordination bonds and reversibility of the dopant [3]. More importantly, this tube-like wrap structure enables ECH-MS/ROP to maintain its favorable para-position with the innate nerve fiber [3].

Taken together, our ECH-MS/ROP delivery system was successfully established, showing satisfactory adhesive, self-curling and electroconductive properties with porous and soft texture and sustained release local anesthetics ability.

3.3. Axonal outgrowth on the ECH-MS/ROP composite

It is well acknowledged that the peripheral nervous system plays a critical role in modulating the movement and sensation of acral tissue [49]. Meanwhile, it can influence the generation, expansion and contraction of peripheral blood vessels and affect cell growth and secretion of nutrients [49]. Promoting peripheral nerve growth and extension is important for diabetic PNI repair. Mounting evidence suggests that ECHs repair central or peripheral nerve injury due to their favorable electrical and mechanical properties similar to the native soft nerve tissue [3,13–15]. Herein, PC12-cells were utilized to further evaluate the therapeutical effect of ECH-MS/ROP on neural cell viability, proliferation, attachment, and axonal outgrowth. The live/dead staining and CCK-8 assay results revealed that the cell viability and proliferation was comparable among three groups (Fig. 3A, B, C). Meanwhile, cytoskeleton imaging exhibited that PC12-cells spread better and interconnected mutually in ECH and ECH-MS/ROP groups, compared to the control group. In addition, the extension area and synaptic length of the PC-12 cells cultured in ECH and ECH-MS/ROP groups were significantly greater than the control group (Fig. 3D and E), which indicated an outstanding cell adhesion-enhancing property of ECH. Furthermore, the relative expression of the axon growth-related genes, which included neurofilaments (NF), growth-associated protein-43 (GAP43), β3-tubulin (TUJ1) and synuclein (SYN), was detected to evaluate the ability of ECH-MS/ROP to stimulate neurite growth. The relative gene expressions of the four markers in the ECH and ECH-MS/ROP groups were comparable and significantly higher than the control group (Fig. 3F and G). In addition, the neural length of PC-12 cells was visualized by NF fluorescence after 3 days of culture on each sample (Fig. 3H). After quantification, neural length in the ECH (59.90 ± 13.89 μm) and ECH-MS/ROP (61.02 ± 11.41 μm) group was comparable, while was significantly longer than the control group (42.54 ± 14.91 μm) (Fig. 3I). Consistently, WB further validated that the expressions of the NF and GAP43 (post-synaptic proteins) in the ECH and ECH-MS/ROP group were significantly higher compared with the control group (Fig. 3J and K). Besides, neuronal neurites of the DRG were further detected to assess the axon-stimulating capacity of the ECH-MS/ROP. Fig. 3L showed that the axonal outgrowth was comparable in the ECH and ECH-MS/ROP group, significantly longer and denser than the control group after 3-day and 7-day culture. After quantification, axon length at day 7 in the ECH (1293.41 ± 120.64 μm) and ECH-MS/ROP (1314.23 ± 124.20 μm) groups was comparable, while was much longer than the blank control group (666.54 ± 181.45 μm) (Fig. 3M). The quantitative axon area showed a consistent tendency with the axon length (Fig. 3M). The above results were consistent with previous reports that the electroconductive PPy could facilitate neural cell proliferation and axon growth via enhancing intercellular transmission through electrical activity [13,49]. Although the application of ROP alone can lead to axonal damage, ECH-MS/ROP in our study demonstrated favorable biocompatibility and the ability to stimulate the neural cell viability and proliferation, likely due to the delayed release of ROP from this system and the positive neural enhancement provided by ECH [50].

3.4. Schwann cell viability, proliferation, attachment and migration on the ECH-MS/ROP composite

It is well-established that Schwann cells are the main gliacyte in the peripheral nervous system, supporting the axons metabolism, affecting the myelination process and forming the nodal domains [3,31]. Thus, viability, proliferation, adhesion, and migration assays for Schwann cells were conducted to examine the myelinated effect of each sample. In accordance with the PC-12 cells results, the ECH-MS/ROP possessed

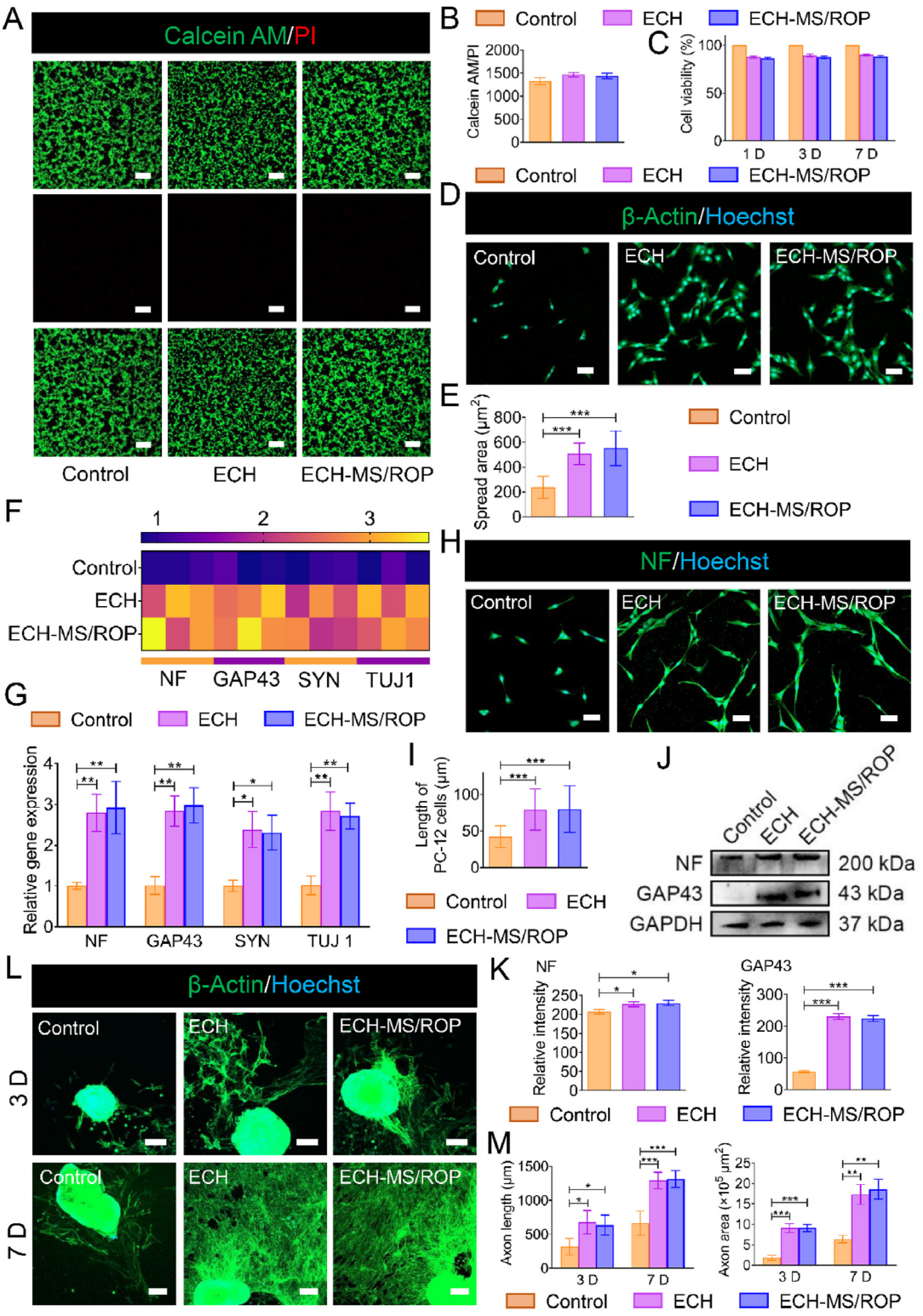

Fig. 3. Axonal outgrowth on the ECH-MS/ROP composite. (A) Live/dead assay of the PC-12 cells cultured on each sample surface for 1 day. Live cells were stained in green and dead cells in red. Scale bar: 200 μm. (B) Quantification of live/dead assay (n = 3). (C) The results of the CCK-8 assay displayed that cell viability exceeded 80% for each sample after seeding for 1, 3 and 7 days (n = 5). (D) The cytoskeleton images showed the attachment of PC-12 cells cultured in each group for 3 days. Scale bar: 50 μm. (E) Quantification of cell spread area (n = 10). (F) A heat map showing the RT-qPCR results on the axon-related gene expressions of PC-12 cells (n = 3). (G) Column graph exhibiting the RT-qPCR results on the axon-related gene expressions in PC-12 cells (n = 3). (H) IF images for the NF (green) and cell nuclei (blue) to observe the axonal extension of the PC-12 cells. Scale bar: 50 μm. (I) Quantification of the axonal lengths of the PC-12 cells on each sample (n = 10). (J) WB analysis detected the protein expressions of NF and GAP43 in PC-12 cells cultured on each sample for 3 days. (K) Protein band intensity was quantified (n = 3). (L) The axonal outgrowth of DRG cultured on each sample for 3 days and 7 days. Scale bar: 200 μm. (M) Analysis of the axon length and area of the DRG for each group (n = 3). Statistical differences were determined by using One-way ANOVA with Bonferroni's multiple comparison tests (*$P < 0.05$, **$P < 0.01$, and ***$P < 0.001$). (For interpretation of the references to colour in this figure legend, the reader is referred to the Web version of this article.)

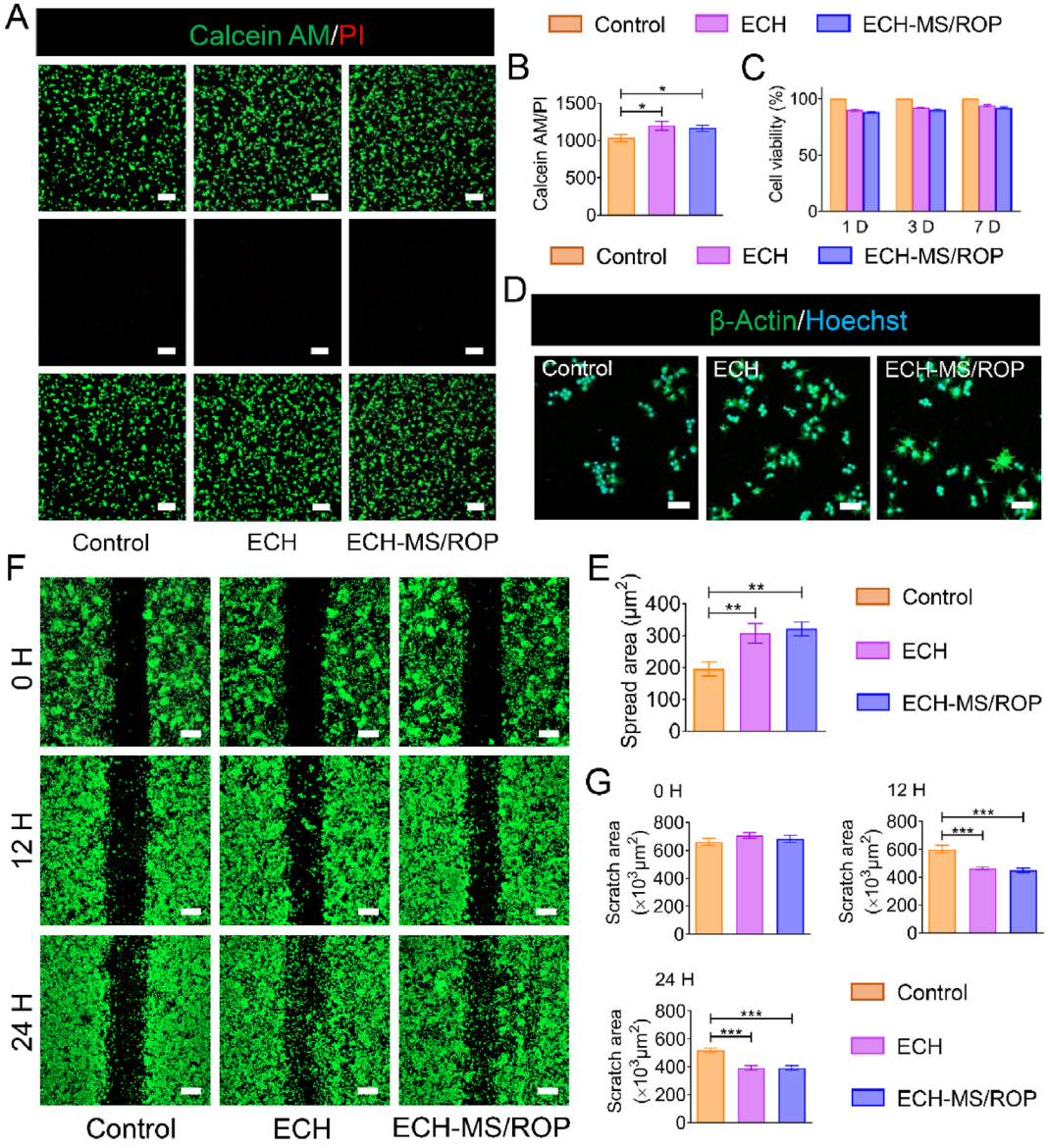

Fig. 4. *In vitro* Schwann cell viability, proliferation, attachment and migration on the ECH-MS/ROP. (A) Live/dead assay of the Schwann cells cultured on each sample surface for 1 day. Live cells were stained in green and dead cells in red. Scale bar: 200 μm. (B) Quantification of live/dead assay (n = 3). (C) The CCK-8 assay displayed that the cell viability exceeded 85% for each sample after seeding for 1, 3 and 7 days (n = 5). (D) The cytoskeleton images showed the attachment of Schwann cells cultured in each group for 3 days. Scale bar: 50 μm. (E) Quantification of cell spread area (n = 10). (F) Wound-healing migration assay of the Schwann cells on each sample at different time points. Scale bar: 200 μm. (G) Quantitative analysis of the scratch area at the denuded site at 0, 12, and 24 h (n = 3). Statistical differences were determined by using One-way ANOVA with Bonferroni's multiple comparison tests (*$P < 0.05$, **$P < 0.01$, and ***$P < 0.001$). (For interpretation of the references to colour in this figure legend, the reader is referred to the Web version of this article.)

great biocompatibility for PC12-cells, as shown by the live/dead and CCK-8 assays (Fig. 4A, B, C). Cytoskeleton micrographs exhibited that Schwann cells cultured on the ECH and ECH-MS/ROP stretched better when compared to the control group, implying that the ECH with or without MS/ROP exhibited satisfactory affinity and adhesion for Schwann cells (Fig. 4D and E). During the cell migration assay, numerous Schwann cells were migrated to the edges and the denuded area after 12 h and 24 h in the ECH and ECH-MS/ROP group (Fig. 4F). Interestingly, Schwann cells could gather at the bare site in the ECH and ECH-MS/ROP and exhibited a disordered arrangement in the control group (Fig. 4F). Additionally, the wound area of the ECH and ECH-MS/ROP group was comparable and significantly lower than the control groups after culture for 12 h and 24 h (Fig. 4G). These findings demonstrated that the ECH and ECH-MS/ROP scaffolds were suitable for cell growth, adhesion and migration, which may be attributed to ECH's hydrophilic and electroconductive properties facilitating the motility of Schwann cells [3,15,51]. Furthermore, the above results revealed that the addition of MS/ROP did not adversely affect the viability and growth of Schwann cells. Although the injection of ROP alone has been reported to potentially induce myelin degeneration and nerve injury, ECH-MS/ROP exhibited desirable biocompatibility and capacity to promote the growth of the myelinated cells, probably due to the slow delivery of ROP from this composite and the beneficial effect of ECH [50].

3.5. *In vivo* biocompatibility examination

Before treatment with ECH-MS/ROP for PNI, *in vivo* biocompatibility was evaluated, including hemocompatibility (hemolytic percentage and serum protein levels) and histological examination of five main organs (heart, lung, liver, spleen and kidney). It is widely recognized that the

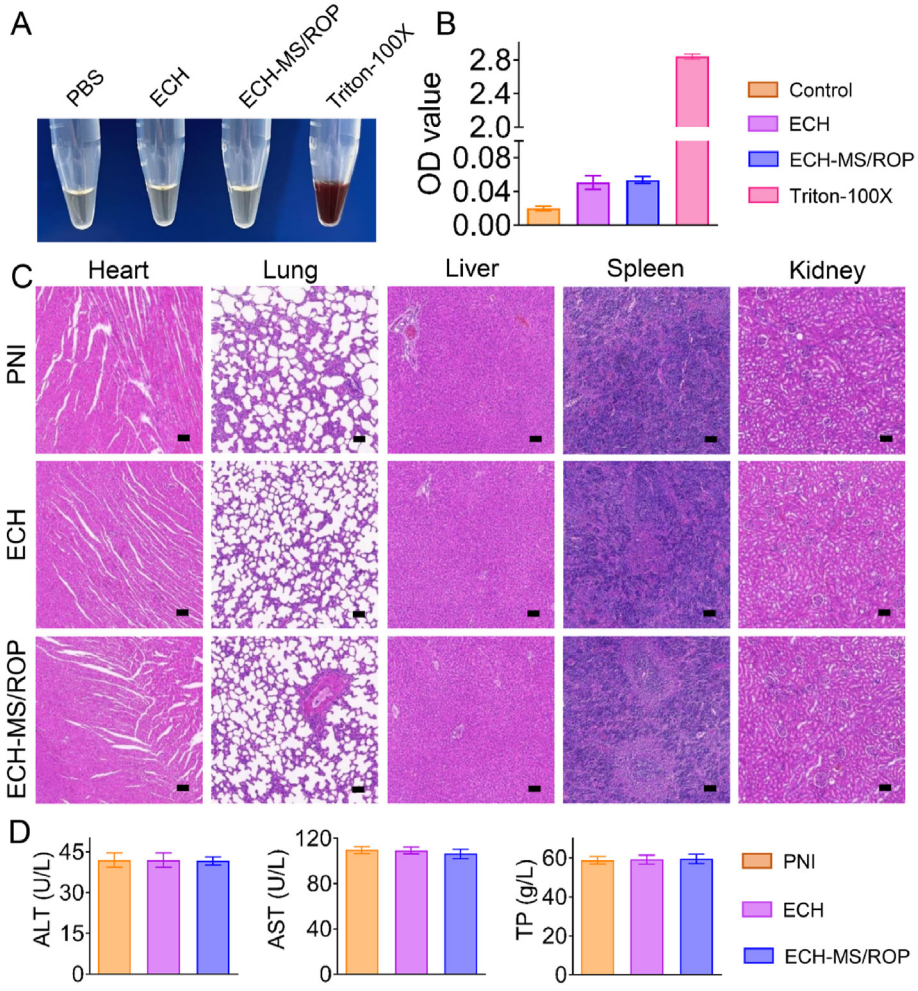

Fig. 5. *In vivo* biocompatibility of ECH-MS/ROP. (A) Photographs of serum obtained from whole blood co-incubated with each sample. Samples including ECH and ECH-MS/ROP were in light yellow and identical to the PBS control group, whereas the Triton-100X group was in bright red, implying its hemolysis. (B) The serum OD values in ECH and ECH-MS/ROP groups were comparable to the PBS group but were significantly lower than the Triton X-100 group (n = 3). (C) HE staining showing normal morphology in the heart, liver, spleen, lung, and kidney tissues from each group. Scale bar: 100 μm. (D) Serum ALT, AST, and TP levels were comparable among different treatment groups, indicating that these hydrogels did not exert systemic toxicity (n = 3). Statistical differences were determined by using One-way ANOVA with Bonferroni's multiple comparison tests (*$P < 0.05$, **$P < 0.01$, and ***$P < 0.001$). (For interpretation of the references to colour in this figure legend, the reader is referred to the Web version of this article.)

hemolytic property is an essential indicator for investigating the hemocompatibility of biomaterials [3,15]. As shown in Fig. 5A, serum obtained from two hydrogels co-incubated with whole blood exhibited faint yellow color, almost identical to the PBS group (negative control), while the Triton-100X group (positive control) was in crimson. The OD value of serum extracted from the two hydrogel groups was similar to the PBS group and significantly lower than the Triton-100X group (Fig. 5B). The hemolytic ratio of both material groups was below 1.2%, suggesting that the ECH-MS/ROP had great hemocompatibility. Additionally, the HE results revealed no significant deposition of degradation products regarding the hydrogel and no abnormal histological changes in the five main organs harvested from animals treated with the hydrogels (Fig. 5C). Moreover, the levels of serum protein (ALT, AST, and TP) were comparable among three groups, indicating ECH-MS/ROP did not yield systemic toxicity (Fig. 5D). Overall, these results indicate that the ECH-MS/ROP is compatible and suitable for *in vivo* application, attributed to its satisfactory biocompatibility [3,13,15,26].

3.6. The ECH-MS/ROP system attenuated pain after diabetic PNI

It is well established that PWT and TWL can quantify mechanical allodynia and thermal hyperalgesia, respectively [36,37,39]. Indeed, increased PWT or TWL suggests attenuated mechanical allodynia or thermal hyperalgesia. Consequently, to verify whether ECH-MS/ROP could exert a long-term analgesic effect after diabetic PNI, PWT (with von-Frey filaments) and TWL (with a hot plate) were tested to evaluate mechanical pain and thermal hyperalgesia (Fig. 6A, D). After PNI, animals treated with ECH alone and without receiving any treatment displayed a significant decrease in PWT from baseline, whereas animals received treatment of ECH-MS/ROP exhibited a significant increase in PWT from baseline (Fig. 6B and C). Notably, PWT in the ECH-MS/ROP group was significantly greater than the ECH and PNI groups after the 8-day treatment, demonstrating that this system could slowly release ROP and exert analgesic effects for up to 8 days (Fig. 6B and C). Similarly, after loading of MS/ROP, the TWL was significantly prolonged, suggesting these rats experienced pain relief (hypoalgesia) (Fig. 6E and F). Although ECHs have been reported to effectively promote nerve regeneration, their application in analgesia after PNI has been largely overlooked [3,13–15]. Moreover, the present study provided compelling evidence that ECH alone could not relieve pain. Therefore, we sought to develop an electroconductive hydrogel to alleviate pain for satisfactory repair after PNI. It is well-established that ROP exhibits an anesthetic effect by blocking the generation and transmission of nerve impulses via reversibly binding the voltage-gated sodium channels on the nerve cell membrane [24,26]. In the present study, ROP was first encapsulated in MS and then loaded in the porous network of ECH to form a sustained delivery system. Indeed, the continuous release of ROP from the ECH-MS/ROP system provided diabetic rats with long-acting analgesia after PNI.

3.7. ECH-MS/ROP enhanced functional recovery after PNI

After validating the analgesic effect of ECH-MS/ROP on PNI, we evaluated its ability to improve functional restoration after diabetic PNI. An experiment based on the SFI was designed to assess functional recovery [3,52]. SFI is a sensitive, reliable, widely-utilized indicator for

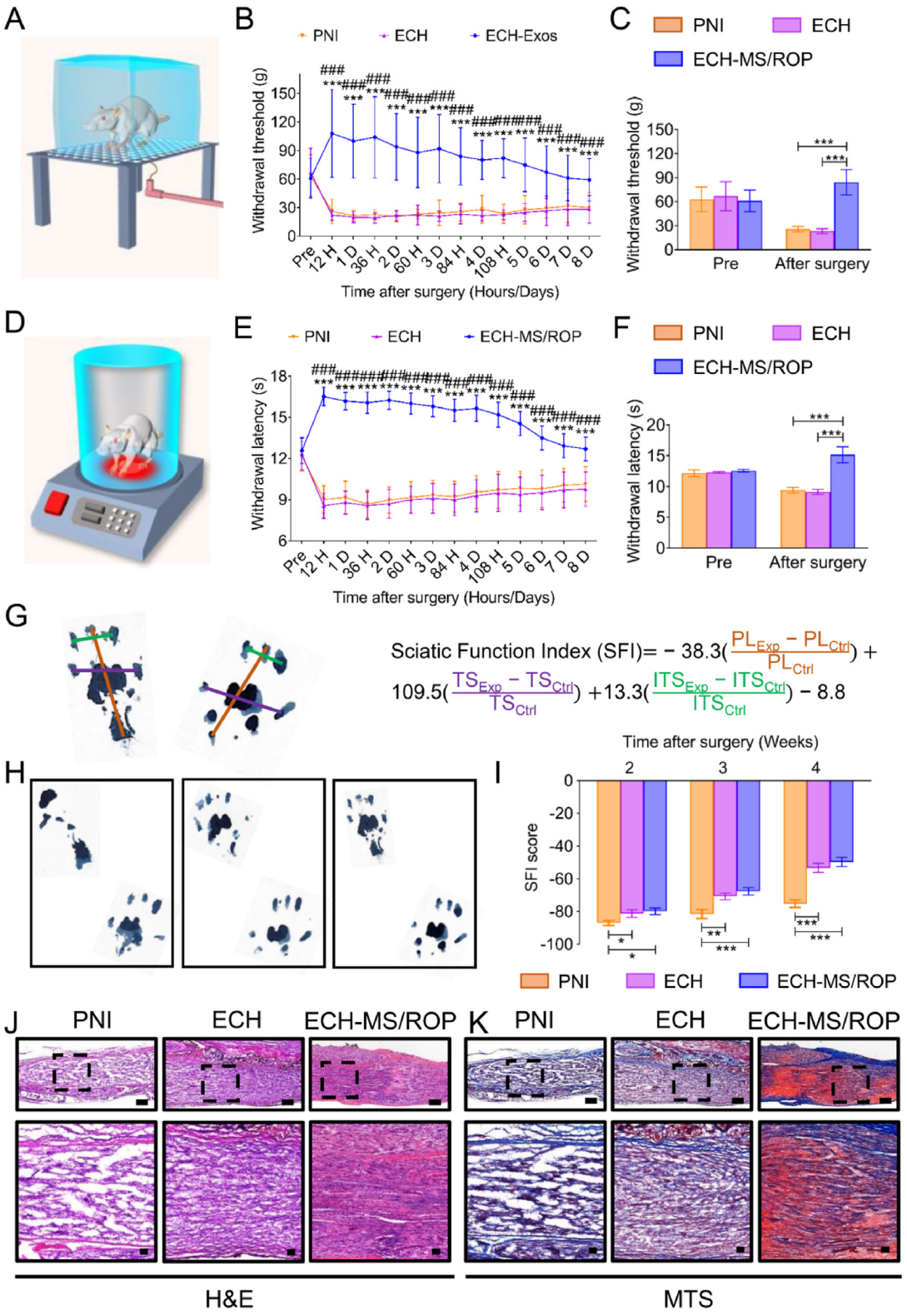

Fig. 6. The ECH-MS/ROP relieved pain and promoted recovery of motor function in diabetic rats after PNI. (A) Schematic diagram depicting the mechanical allodynia assay with von-Frey filaments. (B) Changes in PWT in each group after diabetic PNI compared to baseline (before model establishment) (n = 4). (C) Average PWT of different groups before and after the operation (n = 4). (D) Schematic diagram depicting the thermal hyperalgesia response by hot plate assay. (E) Changes in TWL in each group after diabetic PNI compared to baseline (before model establishment) (n = 4). (F) Average TWL of different groups before and after the operation (n = 4). (G) The equation for calculating the SFI based on different footprint parameters. (H) Representative photographs of the footprints among groups. (I) SFI scores of different treatment groups 2, 3, and 4 weeks after the surgery (n = 3). (J–K) H&E staining and MTS showing sciatic nerve repair after 4 weeks of treatment. Scale bar: 500 μm (at low magnification) and 100 μm (at high magnification). Statistical differences were determined by using the nonparametric Kruskal-Wallis test when analyzing the PWT and TWL or One-way ANOVA with Bonferroni's multiple comparison test when comparing SFI results (* = significantly different from the PNI group, # = significantly different from the ECH group; *, #$P < 0.05$, **, ##$P < 0.01$, and ***, ###$P < 0.001$).

quantitative evaluation of motor function recovery after animal sciatic nerve impairment, which compares footprints of an impaired side with the normal side [3,52]. This index was calculated based on three footprint indicators (PL, TS, and ITS), which ranged from −100 (complete loss of nerve function) to 0 (functional sciatic nerve) (Fig. 6G) [3,52]. Following serious sciatic nerve injury, the nerve and muscle function of the rat's hind limb was seriously impaired. Myelin regeneration and muscle reinnervation gradually occurred, and locomotor function was restored to a certain extent, leading to normal footprints. The rats were placed on a walking track 2 weeks after surgery to collect footprints for SFI scoring. During representative footprint analysis (Fig. 6G and H), after 4 weeks of PNI, the PNI group showed dragged footprints with decreased TS and ITS and increased PL, while rats treated with ECH and ECH-MS/ROP exhibited clear footprints with increased TS and ITS decreased PL. Compared with the PNI group (score = −75.20 ± 2.29), the motor function of rats in the ECH (score = −53.21 ± 2.78) and ECH−MS/ROP (score = −49.64 ± 2.74) groups recovered significantly 4 weeks after treatment (Fig. 6I).

Fig. S2A depicts the establishment of the diabetic PNI model and the therapeutic effect of ECH-MS/ROP. After rats underwent crush injury of the left sciatic nerve, the ECH-MS/ROP dressing was implanted at the injury site and automatically wrapped around tube-like structures (Fig. S2B). Sciatic nerve repair after injury is highly relevant to motor function recovery. Thus, the structural arrangement of the regenerated nerve fiber was visualized by HE and MTS. As observed in Fig. 6J and K, the nerve fibers in the PNI group were discrete, slim, and disarranged, with a significantly injured lesion. Importantly, regenerated nerve fibers in the two treated groups were dense and well organized at the damaged area. Taken together, this ECH-MS/ROP dressing was beneficial for axonal regeneration, restoring locomotor function after diabetic PNI.

3.8. Attenuation of gastrocnemius muscle atrophy

It is widely recognized that alleviated gastrocnemius muscle atrophy indicates locomotor function restoration after sciatic nerve damage. Consequently, appearance evaluations and histological analyses were carried out after 4 weeks of treatment. Indeed, the ipsilateral gastrocnemius muscle (surgical side) was more atrophied than the contralateral one (normal side), especially in the PNI group (Fig. 7A). Further, H&E and MTS examinations for gastrocnemius muscle were conducted to assess histological alterations (Fig. 7B and C). Significant muscle atrophy was observed in the PNI group with slim and disarranged muscle fibers and more collagen deposits. Notably, these adverse outcomes were significantly ameliorated after implantation of the ECH-MS/ROP, yielding plump and well-organized muscle fibers and a few deposited collagen fibers (Fig. 7B and C). After quantification, significantly heavier gastrocnemius muscle and greater muscle fiber density were found in ECH and ECH-MS/ROP groups (Fig. 7D and E). Additionally, the collagen deposition area in the PNI group was approximately 4-fold greater than the ECH and ECH-MS/ROP groups (Fig. 7F). Overall, these results

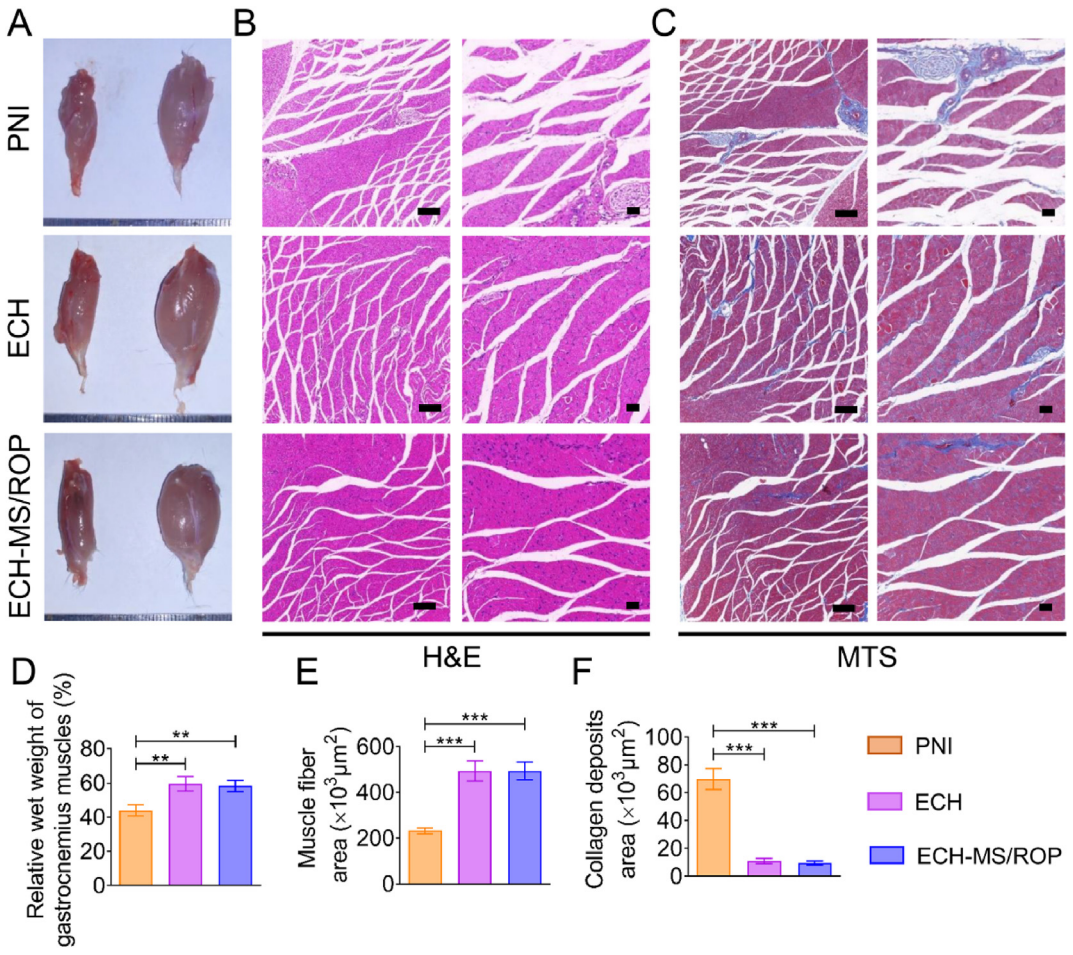

Fig. 7. ECH-MS/ROP treatment attenuated gastrocnemius muscle atrophy. (A) Photographs of the harvested gastrocnemius muscles in each group. (B) HE staining exhibits cross-sectional images of the ipsilateral muscles. Scale bar: 200 μm (at low magnification) and 50 μm (at high magnification). (C) MTS showing the collagen deposits on the cross-sectional images of the ipsilateral muscles. Scale bar: 200 μm (at low magnification) and 50 μm (at high magnification). (D) Quantification of the relative wet weight of the gastrocnemius muscle (n = 3). (E) Quantification of the area of muscle fiber (n = 3). (F) Quantification of the area of collagen deposits (n = 3). Statistical differences were determined by using One-way ANOVA with Bonferroni's multiple comparison tests (*$P < 0.05$, **$P < 0.01$, and ***$P < 0.001$).

verified that the ECH-MS/ROP composite could alleviate muscle atrophy and restore muscle function.

3.9. ECH-MS/ROP promoted axon regeneration and remyelination

Intact nerve fibers and myelin sheath play an important role in the conduction of electrical activity [53]. The myelin-associated axon fibers can grow along the damaged end to both sides of the nerve, thus connecting the two ends of the broken nerve tissue, acting as a "bridge" [54]. Given that NF-200 is a major marker of regenerated axon, IF assay was performed using longitudinal nerve sections to investigate the effect of axon regrowth 4 weeks after surgery. As shown in Fig. 8A, the NF-positive axons were enriched and distributed in order at the damaged site in the ECH and ECH-MS/ROP groups. Moreover, the quantitative analysis results illustrated that the IF intensity was higher and comparable in the ECH and ECH-MS/ROP groups but significantly lower in the PNI group (Fig. 8B). Since myelin basic protein (MBP) is an indicator of remyelination of regenerated axons, nerve sections were stained with this marker to assess myelinated axon regeneration. Similarly, few MBP-positive fibers were observed exhibiting a disordered arrangement in nerves without treatment but were dense and orderly in nerves treated with ECH or ECH-MS/ROP (Fig. 8A). Besides, the fluorescent intensity of MBP was consistent with the NF among three groups (Fig. 8B). Similarly, WB analyses substantiated that the protein levels of NF and MBP in the two treated groups were comparable but were significantly upregulated compared to the PNI group (Fig. 8C and D). The above findings substantiated that ECH-MS/ROP could promote myelinated axon regeneration after diabetic PNI comparable to treatment with ECH alone.

Furthermore, S-100β is a well-recognized marker of remyelination and Schwann cell migration. In this regard, the S-100β positive fibers were well-oriented and distributed regularly ion at the damaged site in the two treated groups (Fig. 8E). In addition, positive S-100β intensity was quantified, and the results showed that positive intensity in the ECH-MS/ROP group was two-fold higher than the PNI group, and comparable to the ECH group, indicating that the Schwann cells played a major role in the growth of myelin sheaths (Fig. 8F). Consistently, WB analysis further verified that S-100β expression level in the two hydrogel-treated groups was significantly higher than the untreated group (Fig. 8G and H). The above results confirmed that the ECH-MS/ROP dressing could effectively promote the regeneration of the myelinated axon. The ECH-MS/ROP hydrogel could promote neural regeneration since this electroconductive hydrogel could connect and recover the impaired nerve at the injury site, thus delivering endogenic bioelectrical signals to the interrupted cells [3,13]. Moreover, it plays an vital role in connecting the upper and lower axons of the injured nerve to the junction [3,13,14].

It is well-established that the MEK/ERK pathway significantly regulates neuronal activity and axonal regeneration [3,14,55]. The bioelectrical signal is important to the activation of this pathway [3]. WB was conducted to quantify the protein expression level of the MEK/ERK signal pathway to investigate the possible mechanisms of ECH-MS/ROP stimulating myelinated axon regeneration. The expression of phosphorylated MEK and ERK was significantly raised in both the hydrogel-treated groups (Fig. 8I and J). However, the unphosphorylated MEK and ERK expression levels were comparable among the three groups (Fig. 8I). Collectively, these findings validated that the ECH-MS/ROP composite facilitated axon myelination and outgrowth via the MEK/ERK signaling pathway.

3.10. TBS and TEM evaluation for axon remyelination

To further assess the remyelination level of the regenerated nerve fiber, TBS and TEM analyses were carried out after preparation of tissue cross-sections. It was observed in the TBS images that medullary sheaths in the none-treated group were messy and sparse, while in the two treated groups were well arranged and dense (Fig. 9A). The TEM results clearly exhibited that the electron-sparse and thin myelin structure irregularly surrounded around the regrown axons in the PNI group, whereas those in the two hydrogel-treated groups were accompanied with electron-dense and thick myelinated sheath structure (Fig. 9B). Interestingly, vacuole-like defects which were a sign of demyelination potentially induced by DM appeared in the myelin sheaths among three groups (Fig. 9B). Additionally, to quantitatively analyze TEM results, four morphological indices, which included the myelinated axon diameter and area, myelin sheath thickness, and G-Ratio, were calculated for comparison [3]. The quantitative results showed that the myelinated axon diameters, myelinated axon area and myelin sheath thickness were comparable in the ECH and ECH-MS/ROP group and were significantly larger than the PNI group (Fig. 9C, D and E). In contrast, the G-Ratio in both the ECH (0.71 ± 0.07) and ECH-MS/ROP group (0.73 ± 0.07) were lower than the PNI group (0.89 ± 0.02) (Fig. 9F). It is reportedly that G-Ratio is relevant to the electroconductive rate and indicates the axon function and integrity, calculated by the ratio of the inner axon diameter to the outer nerve fiber diameter. A greater G-ratio suggests worse remyelination effect of the regrown nerve. Notably, our G-ratio in ECH group (0.71 ± 0.07) or ECH-MS/ROP group (0.73 ± 0.07) was higher than a prior finding (0.60 ± 0.04) that was acquired from young rats without DM and sciatic nerve damage, which is probably attributed to the fact that G-ratio in the this study was obtained from diabetic and injured nerve tissues although receiving favorable treatment [56]. Still, these fingdings verified that the treatment of ECH-MS/ROP could effectively repair injured and demyelinated nerves in rats with DM.

Overall, the *in vivo* studies revealed that the monotherapy with ECH yielded desirable and comparable performance of ECH-MS/ROP for nerve injury repair and recovery of motor function in diabetic rats. Nevertheless, treatment with ECH alone could not overcome the problem of coexisting pain after diabetic PNI. As a powerful local anesthetic, ROP yields favorable analgesic effects by blocking the generation and transmission of nerve impulses via reversibly binding the voltage-gated sodium channels on the nerve cell membrane (Fig. 9G) [24,26]. Nevertheless, a single administration of ROP can potentially induce local and systemic adverse reactions [24–26]. Consequently, ROP was encapsulated in MS and further loaded in the ECH network to achieve long-acting pain relief and meanwhile avoid adverse reactions after diabetic PNI with great biocompatibility and without causing extra nerve impairment. Meanwhile, the ECH-MS/ROP system could promote nerve regeneration and remyelination via MEK/ERK signal pathway, thereby ameliorating denervated muscle atrophy and improving locomotor function in diabetic rats with PNI (Fig. 9G).

4. Conclusion

In this study, we developed an ECH-MS/ROP hydrogel with favorable biocompatibility, excellent conductivity and sustained delivery of local anesthetics for lasting pain relief and nerve regeneration after diabetic PNI. MS/ROP was first prepared by an emulsion-solvent evaporation method. ECH was then synthesized by simply mixing TA, Py, and Fe^{3+}. The MS/ROP were loaded on the ECH network allowing their slow and sustained release and limiting their diffusion away from the lesion site, thereby satisfying the demands for analgesia during early PNI. Notably, the ECH-MS/ROP composite was prepared like a laminar wound or surgical dressing, which could attach to the damaged nerves and automatically wrap around tubular structures, circumventing the need for implantation procedures in cases of diabetic PNI. The capacity of the ECH-MS/ROP to enhance Schwann cell adhesion and migration was confirmed by *in vitro* studies. Additionally, our *in vivo* assays revealed that the ECH-MS/ROP composite could improve mechanical and thermal pain thresholds for long-acting pain relief after diabetic PNI. Moreover, our *in vitro* and *in vivo* results substantiated that the ECH-MS/ROP dressing could facilitate axon regrowth and remyelination through the MEK/ERK signal pathway, further ameliorating denervated muscle atrophy and

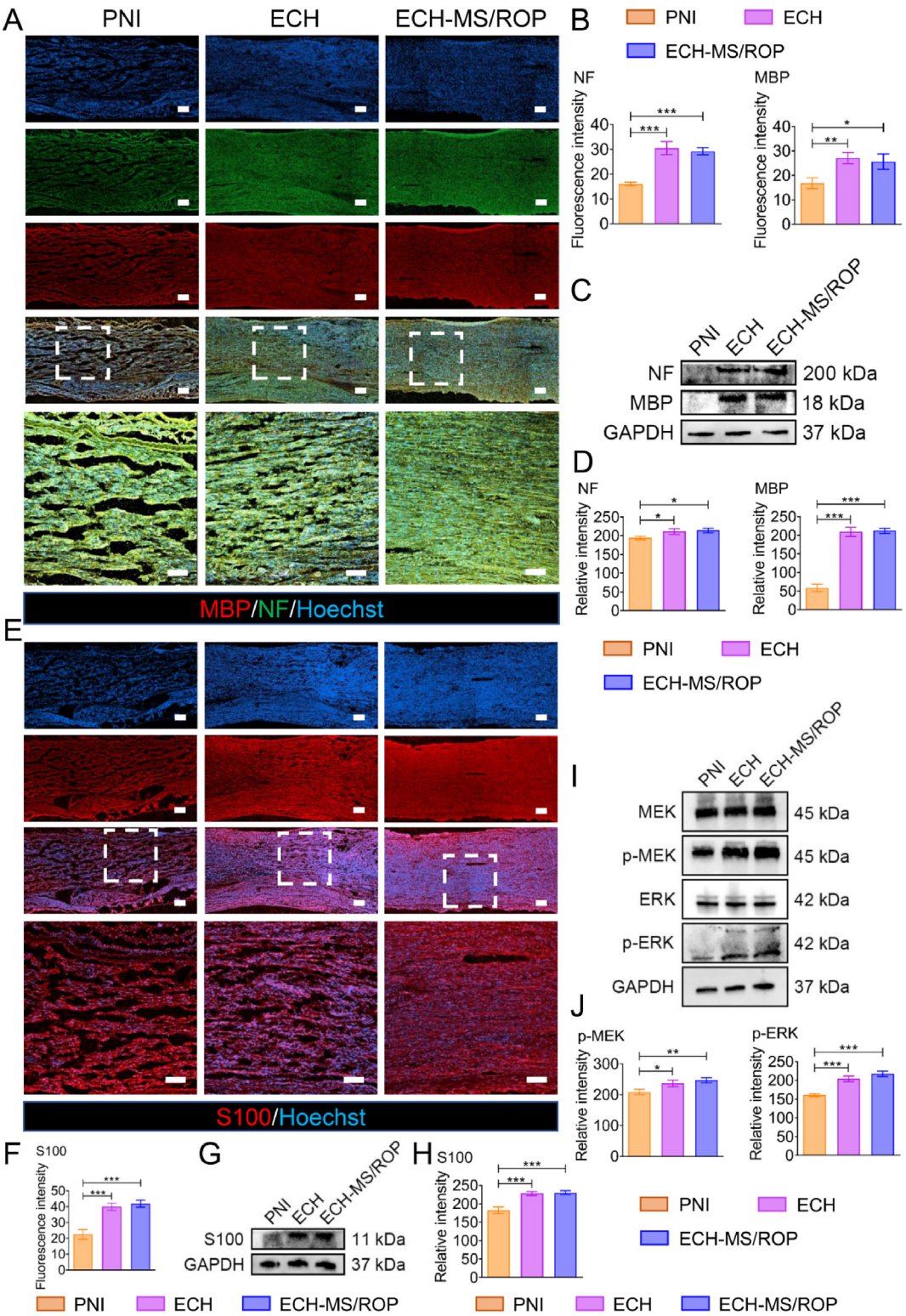

Fig. 8. ECH-MS/ROP treatment promoted axon regrowth and remyelination in diabetic PNI models. (A) IF staining of the NF (green) and MBP (red) proteins in the crushed sciatic nerve tissues after 4 weeks of treatment. Scale bar: 200 μm (at low magnification) and 100 μm (at high magnification). (B) Quantitative analysis of the fluorescence intensity of NF and MBP proteins (n = 3). (C) WB analysis of the proteins expression of *in vivo* NF and MBP. (D) Quantitative analysis of protein band intensity of NF and MBP (n = 3). (E) IF staining of the S100β (red) proteins in the crushed sciatic nerve tissues after 4 weeks of treatment. Scale bar: 200 μm (at low magnification) and 100 μm (at high magnification). (F) Quantitative analysis of the fluorescence intensity of S100β proteins (n = 3). (G) WB analysis of the proteins expression of *in vivo* S100β. (H) Quantitative analysis of protein band intensity of S100β (n = 3). (I) WB analysis of the relative expression of the MEK/ERK pathway proteins. (J) Quantification of the protein band intensity of the MEK/ERK pathway proteins (n = 3). Statistical differences were determined by using One-way ANOVA with Bonferroni's multiple comparison tests (*$P < 0.05$, **$P < 0.01$, and ***$P < 0.001$). (For interpretation of the references to colour in this figure legend, the reader is referred to the Web version of this article.)

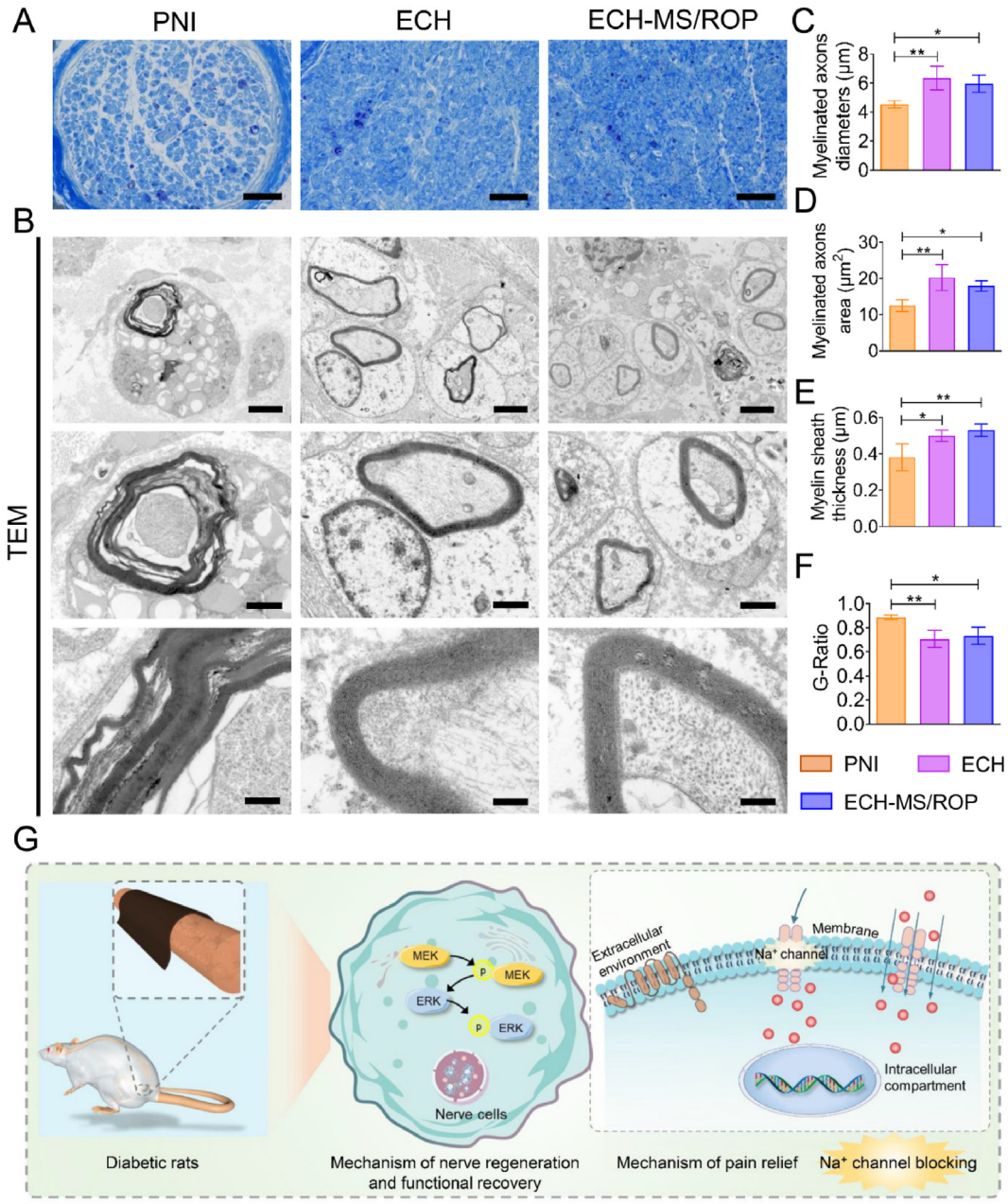

Fig. 9. Morphological evaluation of the axon remyelination using TBS and TEM. (A) TBS showing the remyelination of the regenerated axon. The scale bar represents 50 μm. (B) Representative TEM images of the myelinated axonal regeneration. Scale bar respectively represents 5 μm at low magnification, 2 μm at median magnification and 0.5 μm at high magnification. (C–F) Quantification of the myelination of the regenerated axons with four parameters, including (C) myelinated axon diameter, (D) myelinated axon area, (E) myelin sheath thickness, and (F) G-Ratio (n = 3). (G) The putative mechanism of ECH-MS/ROP in attenuating pain and promoting nerve regeneration and functional restoration after diabetic PNI. Statistical differences were determined by using One-way ANOVA with Bonferroni's multiple comparison test (*$P < 0.05$, **$P < 0.01$, and ***$P < 0.001$).

enhancing locomotor function recovery in diabetic rats with PNI. Overall, our ECH-MS/ROP system has huge prospects for clinical application to stimulate neural regeneration and functional recovery and achieve analgesia after diabetic PNI.

Credit author statement

Fangguo Liang: Conceptualization, Methodology, Resources, Writing – original draft. Yusheng Yang: Formal analysis, Data curation, Writing – review & editing. Yuyong Chen: Software, Visualization. Jiajun Xie: Methodology, Formal analysis. Shencai Liu: Methodology, Validation. Zilin Tan: Methodology, Validation. Liangjie Tian: Software, Visualization. Zhiqiang Yu: Supervision, Writing – review & editing. Zhanjun Shi: Supervision, Writing – review & editing. Peigen Xie: Conceptualization, Methodology, Writing – review & editing. Hong Ding: Validation, Resources. Qinfeng Yang: Conceptualization, Validation, Writing-Review & Editing.

Funding

This work was supported by the President Foundation of Nanfang Hospital, Southern Medical University (2020C024) and the Clinical Research Program of Nanfang Hospital, Southern Medical University (2021CR027).

Declaration of competing interest

The authors declare that they have no known competing financial interests or personal relationships that could have appeared to influence the work reported in this paper.

Data availability

Data will be made available on request.

Acknowledgments

We thank Lei Fan for his help in drawing the schematic diagram and typesetting figures.

Appendix A. Supplementary data

Supplementary data to this article can be found online at https://doi.org/10.1016/j.mtbio.2023.100712.

References

[1] R. Li, Y. Li, Y. Wu, Y. Zhao, H. Chen, Y. Yuan, K. Xu, H. Zhang, Y. Lu, J. Wang, X. Li, X. Jia, J. Xiao, Heparin-poloxamer thermosensitive hydrogel loaded with bFGF and NGF enhances peripheral nerve regeneration in diabetic rats, Biomaterials 168 (2018) 24–37, https://doi.org/10.1016/j.biomaterials.2018.03.044.

[2] T. Lin, S. Liu, S. Chen, S. Qiu, Z. Rao, J. Liu, S. Zhu, L. Yan, H. Mao, Q. Zhu, D. Quan, X. Liu, Hydrogel derived from porcine decellularized nerve tissue as a promising biomaterial for repairing peripheral nerve defects, Acta Biomater. 73 (2018) 326–338, https://doi.org/10.1016/j.actbio.2018.04.001.

[3] C. Liu, L. Fan, Z. Tian, H. Wen, L. Zhou, P. Guan, Y. Luo, C. Chan, G. Tan, C. Ning, L. Rong, B. Liu, Self-curling electroconductive nerve dressing for enhancing peripheral nerve regeneration in diabetic rats, Bioact. Mater. 6 (2021) 3892–3903, https://doi.org/10.1016/j.bioactmat.2021.03.034.

[4] Y. Cai, Q. Huang, P. Wang, K. Ye, Z. Zhao, H. Chen, Z. Liu, H. Liu, H. Wong, M. Tamtaji, K. Zhang, F. Xu, G. Jin, L. Zeng, J. Xie, Y. Du, Z. Hu, D. Sun, J. Qin, X. Lu, Z. Luo, Conductive hydrogel conduits with growth factor gradients for peripheral nerve repair in diabetics with non-suture tape, Adv. Healthc. Mater. 11 (2022) 1–12, https://doi.org/10.1002/adhm.202200755.

[5] J. Zhang, Y. Chen, Y. Huang, W. Wu, X. Deng, H. Liu, R. Li, J. Tao, X. Li, X. Liu, M. Gou, A 3D-printed self-adhesive bandage with drug release for peripheral nerve repair, Adv. Sci. 7 (2020) 1–10, https://doi.org/10.1002/advs.202002601.

[6] H. Samadian, H. Maleki, A. Fathollahi, M. Salehi, S. Gholizadeh, H. Derakhshankhah, Z. Allahyari, M. Jaymand, Naturally occurring biological macromolecules-based hydrogels: potential biomaterials for peripheral nerve regeneration, Int. J. Biol. Macromol. 154 (2020) 795–817, https://doi.org/10.1016/j.ijbiomac.2020.03.155.

[7] S. Vijayavenkataraman, Nerve guide conduits for peripheral nerve injury repair: a review on design, materials and fabrication methods, Acta Biomater. 106 (2020) 54–69, https://doi.org/10.1016/j.actbio.2020.02.003.

[8] A.S. Burahee, A.D. Sanders, C. Shirley, D.M. Power, Cubital tunnel syndrome, EFORT Open Rev 6 (2021) 743–750, https://doi.org/10.1302/2058-5241.6.200129.

[9] T.A. Prest, E. Yeager, S.T. LoPresti, E. Zygelyte, M.J. Martin, L. Dong, A. Gibson, O.O. Olutoye, B.N. Brown, J. Cheetham, Nerve-specific, xenogeneic extracellular matrix hydrogel promotes recovery following peripheral nerve injury, J. Biomed. Mater. Res. A. 106 (2018) 450–459, https://doi.org/10.1002/jbm.a.36235.

[10] A. Baron, A. Strohl, Severe cubital tunnel syndrome: considerations for nerve transfer surgery, Curr. Rev. Musculoskelet. Med. 13 (2020) 708–716, https://doi.org/10.1007/s12178-020-09676-2.

[11] B. Fan, M. Chopp, Z.G. Zhang, X.S. Liu, Treatment of diabetic peripheral neuropathy with engineered mesenchymal stromal cell-derived exosomes enriched with microRNA-146a provide amplified therapeutic efficacy, Exp. Neurol. 341 (2021), 113694, https://doi.org/10.1016/j.expneurol.2021.113694.

[12] B. Zhao, Q. Zhang, X. Liang, J. Xie, Q. Sun, Quercetin reduces inflammation in a rat model of diabetic peripheral neuropathy by regulating the TLR4/MyD88/NF-κB signalling pathway, Eur. J. Pharmacol. 912 (2021), 174607, https://doi.org/10.1016/j.ejphar.2021.174607.

[13] L. Zhou, L. Fan, X. Yi, Z. Zhou, C. Liu, R. Fu, C. Dai, Z. Wang, X. Chen, P. Yu, D. Chen, G. Tan, Q. Wang, C. Ning, Soft conducting polymer hydrogels cross-linked and doped by tannic acid for spinal cord injury repair, ACS Nano 12 (2018) 10957–10967, https://doi.org/10.1021/acsnano.8b04609.

[14] Y. Luo, L. Fan, C. Liu, H. Wen, S. Wang, P. Guan, D. Chen, C. Ning, L. Zhou, G. Tan, An injectable, self-healing, electroconductive extracellular matrix-based hydrogel for enhancing tissue repair after traumatic spinal cord injury, Bioact. Mater. 7 (2022) 98–111, https://doi.org/10.1016/j.bioactmat.2021.05.039.

[15] L. Fan, C. Liu, X. Chen, L. Zheng, Y. Zou, H. Wen, P. Guan, F. Lu, Y. Luo, G. Tan, P. Yu, D. Chen, C. Deng, Y. Sun, L. Zhou, C. Ning, Exosomes-loaded electroconductive hydrogel synergistically promotes tissue repair after spinal cord injury via immunoregulation and enhancement of myelinated axon growth, Adv. Sci. 9 (2022) 1–22, https://doi.org/10.1002/advs.202105586.

[16] Y. Qian, Y. Cheng, J. Song, Y. Xu, W.-E. Yuan, C. Fan, X. Zheng, Mechano-informed biomimetic polymer scaffolds by incorporating self-powered zinc oxide nanogenerators enhance motor recovery and neural function, Small 16 (2020), e2000796, https://doi.org/10.1002/smll.202000796.

[17] R. Lorenzoni, R.V. Contri, C.K.F. de Lima, F. Barreto, B.V. de Araujo, A.R. Pohlmann, A.L.P. de Miranda, T.D. Costa, S.S. Guterres, Dermatopharmacokinetic and pharmacodynamic evaluation of a novel nanostructured formulation containing capsaicinoids for treating neuropathic pain, Int. J. Pharm. 596 (2021), 120294, https://doi.org/10.1016/j.ijpharm.2021.120294.

[18] W.L. Dai, B. Yan, Y.N. Bao, J.F. Fan, J.H. Liu, Suppression of peripheral NGF attenuates neuropathic pain induced by chronic constriction injury through the TAK1-MAPK/NF-κB signaling pathways, Cell Commun. Signal. 18 (2020) 1–13, https://doi.org/10.1186/s12964-020-00556-3.

[19] F.R. Santos Passos, E.W.M. Pereira, L. Heimfarth, B.S. Monteiro, Y.M. Barbosa Gomes de Carvalho, P.S. Siqueira-Lima, H.D. Melo Coutinho, A. Antunes de Souza Araújo, J.R. Guedes da Silva Almeida, R.S.S. Barreto, L. Picot, L.J. Quintans-Júnior, J.S.S. Quintans, Role of peripheral and central sensitization in the anti-hyperalgesic effect of hecogenin acetate, an acetylated sapogenin, complexed with β-cyclodextrin: involvement of NFκB and p38 MAPK pathways, Neuropharmacology 186 (2021), 108395, https://doi.org/10.1016/j.neuropharm.2020.108395.

[20] C. Wen, M. Xu, C. Mo, Z. Cheng, Q. Guo, X. Zhu, JMJD6 exerts function in neuropathic pain by regulating NF-κB following peripheral nerve injury in rats, Int. J. Mol. Med. 42 (2018) 633–642, https://doi.org/10.3892/ijmm.2018.3613.

[21] L.W. Chu, K.I. Cheng, J.Y. Chen, Y.C. Cheng, Y.C. Chang, J.L. Yeh, J.H. Hsu, Z.K. Dai, B.N. Wu, Loganin prevents chronic constriction injury-provoked neuropathic pain by reducing TNF-α/IL-1β-mediated NF-κB activation and Schwann cell demyelination, Phytomedicine 67 (2020), 153166, https://doi.org/10.1016/j.phymed.2019.153166.

[22] J.M. Nichols, C.V. Crelli, L. Liu, H.V. Pham, J.M. Janjic, A.J. Shepherd, Tracking macrophages in diabetic neuropathy with two-color nanoemulsions for near-infrared fluorescent imaging and microscopy, J. Neuroinflammation 18 (2021) 1–22, https://doi.org/10.1186/s12974-021-02365-y.

[23] T. Xue, X. Zhang, Y. Xing, S. Liu, L. Zhang, X. Wang, M. Yu, Advances about immunoinflammatory pathogenesis and treatment in diabetic peripheral neuropathy, Front. Pharmacol. 12 (2021) 1–10, https://doi.org/10.3389/fphar.2021.748193.

[24] W. Zhang, W. Xu, C. Ning, M. Li, G. Zhao, W. Jiang, J. Ding, X. Chen, Long-acting hydrogel/microsphere composite sequentially releases dexmedetomidine and bupivacaine for prolonged synergistic analgesia, Biomaterials 181 (2018) 378–391, https://doi.org/10.1016/j.biomaterials.2018.07.051.

[25] W. Zhang, C. Ning, W. Xu, H. Hu, M. Li, G. Zhao, J. Ding, X. Chen, Precision-guided long-acting analgesia by hydrogel-immobilized bupivacaine-loaded microsphere, Theranostics 8 (2018) 3331–3347, https://doi.org/10.7150/thno.25276.

[26] M. Khanal, S.V. Gohil, E. Kuyinu, H.M. Kan, B.E. Knight, K.M. Baumbauer, K.W.H. Lo, J. Walker, C.T. Laurencin, L.S. Nair, Injectable nanocomposite analgesic delivery system for musculoskeletal pain management, Acta Biomater. 74 (2018) 280–290, https://doi.org/10.1016/j.actbio.2018.05.038.

[27] K. Pachis, S. Blazaki, M. Tzatzarakis, P. Klepetsanis, E. Naoumidi, M. Tsilimbaris, S.G. Antimisiaris, Sustained release of intravitreal flurbiprofen from a novel drug-in-liposome-in-hydrogel formulation, Eur. J. Pharmaceut. Sci. 109 (2017) 324–333, https://doi.org/10.1016/j.ejps.2017.08.028.

[28] X. Zhao, Y. Gao, X. Tang, W. Lei, Y. Yang, F. Yu, Y. Liu, M. Yang, Y. Wang, W. Gong, Z. Li, C. Gao, X. Mei, Development and evaluation of ropivacaine loaded poly(lactic-Co-glycolic acid) microspheres with low burst release, Curr. Drug Deliv. 16 (2019) 490–499, https://doi.org/10.2174/1567201816666190528122137.

[29] X. Tian, H. Zhu, S. Du, X.Q. Zhang, F. Lin, F. Ji, Y.H. Tsou, Z. Li, Y. Feng, K. Ticehurst, S. Hannaford, X. Xu, Y.X. Tao, Injectable PLGA-coated ropivacaine produces A long-lasting analgesic effect on incisional pain and neuropathic pain, J. Pain 22 (2021) 180–195, https://doi.org/10.1016/j.jpain.2020.03.009.

[30] Q. Yang, S. Su, S. Liu, S. Yang, J. Xu, Y. Zhong, Y. Yang, L. Tian, Z. Tan, J. Wang, Z. Yu, Z. Shi, F. Liang, Exosomes-loaded electroconductive nerve dressing for nerve regeneration and pain relief against diabetic peripheral nerve injury, Bioact. Mater 26 (2023) 194–215, https://doi.org/10.1016/j.bioactmat.2023.02.024.

[31] N.P. Gonçalves, C.B. Vægter, H. Andersen, L. Østergaard, N.A. Calcutt, T.S. Jensen, Schwann cell interactions with axons and microvessels in diabetic neuropathy, Nat. Rev. Neurol. 13 (2017) 135–147, https://doi.org/10.1038/nrneurol.2016.201.

[32] Q. Min, D.B. Parkinson, X.-P. Dun, Migrating Schwann cells direct axon regeneration within the peripheral nerve bridge, Glia 69 (2021) 235–254, https://doi.org/10.1002/glia.23892.

[33] Y. Wang, F. Zhang, Y. Zhang, Q. Shan, W. Liu, F. Zhang, F. Zhang, S. Yi, Betacellulin regulates peripheral nerve regeneration by affecting Schwann cell migration and axon elongation, Mol. Med. 27 (2021) 27, https://doi.org/10.1186/s10020-021-00292-5.

[34] L. Chen, Z. Chen, Z. Xu, W. Feng, X. Yang, Z. Qi, Polydatin protects Schwann cells from methylglyoxal induced cytotoxicity and promotes crushed sciatic nerves regeneration of diabetic rats, Phyther. Res. 35 (2021) 4592–4604, https://doi.org/10.1002/ptr.7177.

[35] T.L. Lopez-Silva, C.D. Cristobal, C.S. Edwin Lai, V. Leyva-Aranda, H.K. Lee, J.D. Hartgerink, Self-assembling multidomain peptide hydrogels accelerate peripheral nerve regeneration after crush injury, Biomaterials 265 (2021), 120401, https://doi.org/10.1016/j.biomaterials.2020.120401.

[36] H.M. Guo, Y. Zhang, Y. Zhang, P.F. Jiao, X.C. Fan, C.L. Kong, T. Wang, X.X. Li, H.W. Zhang, L.R. Zhang, M.Y. Ma, H.L. Bu, Spinal Ninjurin2 contributes to the

neuropathic pain via NF-κB-mediated neuroinflammation in the spared sciatic nerve injury rats, Int. Immunopharm. 99 (2021), 107918, https://doi.org/10.1016/j.intimp.2021.107918.
[37] N.M. Elsherbiny, E. Ahmed, G.A. Kader, Y. Abdel-mottaleb, M.H. ElSayed, A.M. Youssef, S.A. Zaitone, Inhibitory effect of valproate sodium on pain behavior in diabetic mice involves suppression of spinal histone deacetylase 1 and inflammatory mediators, Int. Immunopharm. 70 (2019) 16–27, https://doi.org/10.1016/j.intimp.2019.01.050.
[38] T. Suto, H. Obata, M. Tobe, H. Oku, H. Yokoo, Y. Nakazato, S. Saito, Long-term effect of epidural injection with sustained-release lidocaine particles in a rat model of postoperative pain, Br. J. Anaesth. 109 (2012) 957–967, https://doi.org/10.1093/bja/aes302.
[39] X. Gao, P. Zhu, L. Yu, L. Yang, Y. Chen, Ultrasound/acidity-triggered and nanoparticle-enabled analgesia, Adv. Healthc. Mater. 8 (2019) 1–10, https://doi.org/10.1002/adhm.201801350.
[40] Z. Yao, W. Yuan, J. Xu, W. Tong, J. Mi, P.C. Ho, D.H.K. Chow, Y. Li, H. Yao, X. Li, S. Xu, J. Guo, Q. Zhu, L. Bian, L. Qin, Magnesium-encapsulated injectable hydrogel and 3D-engineered polycaprolactone conduit facilitate peripheral nerve regeneration, Adv. Sci. 9 (2022) 1–16, https://doi.org/10.1002/advs.202202102.
[41] Li Ye, J. Xu, J. Mi, X. He, Q. Pan, L. Zheng, H. Zu, Z. Chen, B. Dai, X. Li, Q. Pang, L. Zou, L. Zhou, L. Huang, W. Tong, G. Li, L. Qin, Biodegradable magnesium combined with distraction osteogenesis synergistically stimulates bone tissue regeneration via CGRP-FAK-VEGF signaling axis, Biomaterials 275 (2021), 120984, https://doi.org/10.1016/j.biomaterials.2021.120984.
[42] W. yong Zhu, J. Guo, W. fa Yang, Z. ying Tao, X. Lan, L. Wang, J. Xu, L. Qin, Y. xiong Su, Biodegradable magnesium implant enhances angiogenesis and alleviates medication-related osteonecrosis of the jaw in rats, J. Orthop. Transl. 33 (2022) 153–161, https://doi.org/10.1016/j.jot.2022.03.004.
[43] Y. Wang, X. Wang, X. Wang, Y. Song, X. Wang, J. Hao, Design and development of lidocaine microemulsions for transdermal delivery, AAPS PharmSciTech 20 (2019) 1–9, https://doi.org/10.1208/s12249-018-1263-1.
[44] L.N.M. Ribeiro, M. Franz-Montan, M.C. Breitkreitz, A.C.S. Alcântara, S.R. Castro, V.A. Guilherme, R.M. Barbosa, E. de Paula, Nanostructured lipid carriers as robust systems for topical lidocaine-prilocaine release in dentistry, Eur. J. Pharmaceut. Sci. 93 (2016) 192–202, https://doi.org/10.1016/j.ejps.2016.08.030.
[45] W. Zeng, H. Hui, Z. Liu, Z. Chang, M. Wang, B. He, D. Hao, TPP ionically cross-linked chitosan/PLGA microspheres for the delivery of NGF for peripheral nerve system repair, Carbohydr, Polym 258 (2021), 117684, https://doi.org/10.1016/j.carbpol.2021.117684.
[46] B. Wu, L. Wu, Y. He, Z. Yin, L. Deng, Engineered PLGA microspheres for extended release of brexpiprazole: in vitro and in vivo studies, Drug Dev. Ind. Pharm. 47 (2021) 1001–1010, https://doi.org/10.1080/03639045.2021.1934859.
[47] P. Wang, X. Zhuo, W. Chu, X. Tang, Exenatide-loaded microsphere/thermosensitive hydrogel long-acting delivery system with high drug bioactivity, Int. J. Pharm. 528 (2017) 62–75, https://doi.org/10.1016/j.ijpharm.2017.05.069.
[48] X. Zhao, C. Fan, J. Wang, H. Xiong, T. Zhu, Y. Liu, H. Pan, W. Weijia Lu, Bioinspired multichannel nerve guidance conduit based on shape memory nanofibers for potential application in peripheral nerve repair, ACS Nano 14 (2020) 12579–12595, https://doi.org/10.1021/acsnano.0c03570.
[49] X. Zhang, W. Qu, D. Li, K. Shi, R. Li, Y. Han, E. Jin, J. Ding, X. Chen, Functional polymer-based nerve guide conduits to promote peripheral nerve regeneration, Adv. Mater. Interfac. 7 (2020) 1–21, https://doi.org/10.1002/admi.202000225.
[50] B.S. Kim, J.H. Choi, S.H. Baek, D.H. Lee, Effects of intraneural injection of dexmedetomidine in combination with ropivacaine in rat sciatic nerve block, Reg. Anesth. Pain Med. 43 (2018) 378–384, https://doi.org/10.1097/AAP.0000000000000745.
[51] L. Fan, C. Xiao, P. Guan, Y. Zou, H. Wen, C. Liu, Y. Luo, G. Tan, Q. Wang, Y. Li, P. Yu, L. Zhou, C. Ning, Extracellular matrix-based conductive interpenetrating network hydrogels with enhanced neurovascular regeneration properties for diabetic wounds repair, Adv. Healthc. Mater. 11 (2022), e2101556, https://doi.org/10.1002/adhm.202101556.
[52] N. Mirzakhani, A.A. Farshid, E. Tamaddonfard, M. Imani, A. Erfanparast, F. Noroozinia, Carnosine improves functional recovery and structural regeneration after sciatic nerve crush injury in rats, Life Sci. 215 (2018) 22–30, https://doi.org/10.1016/j.lfs.2018.10.043.
[53] R.N. Fernando, L. Cotter, C. Perrin-Tricaud, J. Berthelot, S. Bartolami, J.A. Pereira, S. Gonzalez, U. Suter, N. Tricaud, Optimal myelin elongation relies on YAP activation by axonal growth and inhibition by Crb3/Hippo pathway, Nat. Commun. 7 (2016), https://doi.org/10.1038/ncomms12186.
[54] T. Führmann, P.N. Anandakumaran, M.S. Shoichet, Combinatorial therapies after spinal cord injury: how can biomaterials help? Adv. Healthc. Mater. 6 (2017) 1–21, https://doi.org/10.1002/adhm.201601130.
[55] T.D. Glenn, W.S. Talbot, Signals regulating myelination in peripheral nerves and the Schwann cell response to injury, Curr. Opin. Neurobiol. 23 (2013) 1041–1048, https://doi.org/10.1016/j.conb.2013.06.010.
[56] M.B. Christensen, P.A. Tresco, Differences exist in the left and right sciatic nerves of naïve rats and cats, Anat. Rec. 298 (2015) 1492–1501, https://doi.org/10.1002/ar.23161.